2012

Neutrino data analysis using the side muon range detector (SMRD) of the Tokai to Kamiokande (T2K) long baseline neutrino experiment

Jeremiah John Haremza
Louisiana State University and Agricultural and Mechanical College, jharem1@lsu.edu

NEUTRINO DATA ANALYSIS USING THE SIDE MUON RANGE DETECTOR (SMRD) OF THE TOKAI TO KAMIOKANDE (T2K) LONG BASELINE NEUTRINO OSCILLATION EXPERIMENT

A Thesis

Submitted to the Graduate Faculty of the
Louisiana State University and
Agricultural and Mechanical College
requirements for the degree of
Master of Science

in

The Department of Physics & Astronomy

by
Jeremiah J. Haremza
B.S., University of Rochester, 2009
B.A., University of Rochester, 2009
August 2012

Acknowledgments

Although a complete and exhaustive list of people I wish to thank is difficult to complete, as it is always possible to forget someone, I will make my best effort to include those most directly involved in the development of this thesis.

I would like to thank those individuals from whom I have learned so much while working in the T2K data quality group including Nick Hastings, Francesca Di Lodovico, Roberto Sacco, Takatomi Yano, and Martin Haigh.

In addition I would like to thank those in the research group here at LSU including Bill Metcalf, Oleg Perevozchikov, Jerry Coleman, Martin Tzanov, and Johathan Insler.

I want to also acknowledge the service of the the members of the thesis defense committee including Jim Matthews and Jeff Blackmon. In addition I would like to acknowledge not only the classroom instruction I received from Dr. Blackmon but also his help in continuing my academic career.

Last and most importantly I would like to thank Thomas Kutter for his service as my thesis adviser and for his general instruction and guidance. He has helped tremendously in regards to continuing my career in the sciences and to preparation to do such.

Table of Contents

List of Tables

List of Figures

Abstract

In this thesis we describe data quality considerations for the Side Muon Rang Detector (SMRD), one of the six sub-detectors of the ND280 near detector of the Tokai to Kamiokande (T2K) long baseline neutrino oscillation experiment. Herein we show that the data quality of the SMRD has taken good data 99.9584% of the time it has been recording data. Also, 99.676% of SMRD data channels are shown to be operating optimally. In addition we discuss the stability of the SMRD. We find that based on a subset of data unbiased cosmic triggers have light yield of 112.8 ± 0.3 p.e. vs. 100.7 ± 0.5 p.e. for vertical and horizontal counters respectively. For a more stringent data set cosmic light yield for tracks with a nearly vertical path is determined to be 79.6 ± 0.5 p.e. Detector stability is found to be related to the applied cosmic trigger mask, and this is evidenced in the increased stability of Run II over that of Run I. Also included is a basic introduction to neutrino physics and an overview of the T2K experiment.

Chapter 1

Introduction

1.1 Pauli Proposes the Neutrino

Historically, the study of β-decay provided the first physical evidence of the neutrino. In 1911 Lise Meitner and Otto Hahn performed an experiment that showed that the energies of electrons emitted by β-decay had a continuous rather than discrete spectrum. During the years 1920-1927, Charles Drummond Ellis (along with James Chadwick and colleagues) established clearly that the β-decay spectrum is really continuous, ending all controversies as to whether or not the energy spectrum was continuous [2].

At the time of these experiments only the electron and the recoiling daughter nucleus were observed in β-decay. Therefore, the process was assumed to be a two body disintegration akin to α-decay. Thus, for a β-decay represented as follows:

$$ {}^{\mathrm{A}}_{\mathrm{Z}}\mathrm{X} \longrightarrow {}_{\mathrm{Z+1}}{}^{\mathrm{A}}\mathrm{Y} + e^{-} \tag{1.1} $$

where the parent nucleus is at rest, conservation of energy requires

$$ E_X = E_Y + E_{e^-} = E_Y + T_{e^-} + m_e c^2 \tag{1.2} $$

or

$$ T_{e^-} = (E_X - E_Y - m_e c^2) = (M_X - M_Y - m_e)c^2 - T_Y = Q - T_Y \approx Q \tag{1.3} $$

where we have defined the disintegration energy or Q-value as the difference between the rest masses of the initial and final states. It is also clear that Q can be equated with the sum of the kinetic energies of the final two particles. However, the electron is expected to carry away the vast majority of the released energy, as it is the lighter of the two resulting particles, and thus $T_{e^-} >> T_Y$. What is most important here is that the above two body kinematic analysis shows a discrete resulting energy for the electron.

But the experimental evidence did not measure a discrete energy for the emitted β particles. Instead a continuous spectrum of energies, as shown in Fig. 1.1, up to the expected discrete energy of the Q-value were experimentally measured. This was in apparent contradiction to the law of conservation of energy, as it appeared that energy was lost in the β-decay process.

This discrepancy in the electron energy spectrum was not the only problem. Upon examination of Eq. 1.1 it is easily noticed that the number of nucleons does not change in the decay, i.e. $\Delta A = 0$. There is, however, a fermion emitted in the process - the emitted electron. Now, both the nucleons and the electron have angular momentum equal to $\hbar/2$. Hence, regardless of any change in orbital angular momentum, which must itself have an integral value, the angular momentum is clearly not conserved.

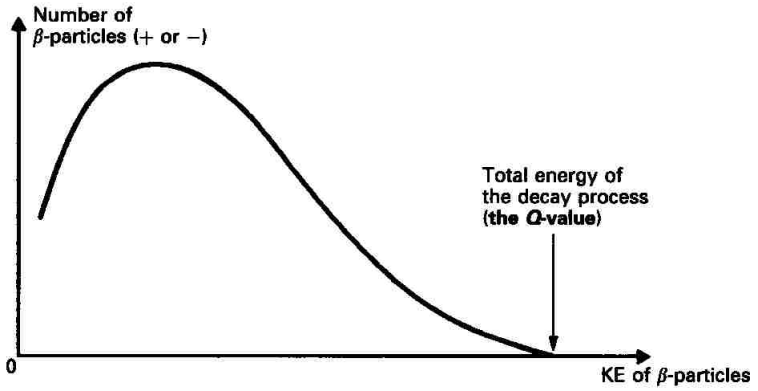

Figure 1.1: experimentally observed continuous energy spectrum of emitted β particles.

Similar analyses, both kinematic and for angular momentum, can be done for the other 2 forms of β-deacy - positron emission and electron capture represented by Eq. 1.4 and 1.5.

$$ {}^{\mathrm{A}}_{\mathrm{Z}}\mathrm{X} \longrightarrow {}_{\mathrm{Z}-1}{}^{\mathrm{A}}\mathrm{Y} + e^{+} \tag{1.4} $$

$$ {}^{\mathrm{A}}_{\mathrm{Z}}\mathrm{X} + e^{-} \longrightarrow {}_{\mathrm{Z}-1}{}^{\mathrm{A}}\mathrm{Y} \tag{1.5} $$

In his now famous letter, dated December 4^{th} 1930, Wolfgang Pauli suggested that in addition to electrons and protons atoms also contained an extremely light neutral particle which he called the neutron [3]. He suggested that this "neutron" was also emitted during β-decay and had simply not yet been observed. Pauli hypothesized that this new particle had spin ½, obeyed the exclusion principle, traveled at a velocity less than that of light, and had a mass the order of the electron but not larger than 0.01 proton masses.

Designating our new particle ν and its corresponding antiparticle $\bar{\nu}$, Eq. 1.1, 1.4, and 1.5 would be rewritten as

$$ \begin{aligned} {}^{\mathrm{A}}_{\mathrm{Z}}\mathrm{X} &\longrightarrow {}_{\mathrm{Z}+1}{}^{\mathrm{A}}\mathrm{Y} + e^{-} + \bar{\nu} \\ {}^{\mathrm{A}}_{\mathrm{Z}}\mathrm{X} &\longrightarrow {}_{\mathrm{Z}-1}{}^{\mathrm{A}}\mathrm{Y} + e^{+} + \nu \\ {}^{\mathrm{A}}_{\mathrm{Z}}\mathrm{X} + e^{-} &\longrightarrow {}_{\mathrm{Z}-1}{}^{\mathrm{A}}\mathrm{Y} + \nu \end{aligned} \tag{1.6} $$

Adjusting the above two-body kinematic analysis shown in Eq. 1.2 for the three-body electron emission in Eq. 1.6, and assuming the parent nucleus starts at rest, yields

$$\begin{aligned} M_P c^2 &= T_D + M_D c^2 + T_{e^-} + m_e c^2 + T_{\bar{\nu}} + m_{\bar{\nu}} c^2 \\ (M_P - M_D - m_e - m_{\bar{\nu}})c^2 &= T_D + T_{e^-} + T_{\bar{\nu}} \\ &= \Delta M c^2 = Q \end{aligned} \tag{1.7}$$

where M_P, M_D, m_e, and $m_{\bar{\nu}}$ are the masses of the parent nucleus, the daughter nucleus, the electron, and the "neutron". Similarly, T_D, T_{e^-}, and $T_{\bar{\nu}}$ represent the kinetic energies of the daughter nucleus, the electron, and the "neutron".

Once again, because the daughter nucleus is much more massive than either the electron or the "netron", the recoil energy of the daughter nucleus maybe ignored, and for any β-decay we can write

$$T_{e^-} + T_{\bar{\nu}} \approx Q \tag{1.8}$$

Clearly then, in the three-body kinematic analysis, the kinetic energy of the electron is no longer discrete. Instead, any continuous value $0 \leq T_{e^-} \geq Q$ is kinematically allowed, and the maximum electron energy, corresponding to $T_{\bar{\nu}} = 0$, is given by the endpoint value of Eq. 1.7

$$(T_{e^-})_{max} = Q \tag{1.9}$$

Thus, Pauli's postulated particle resolves the problem of the continuous energy spectrum in β-decay, while simultaneously restoring all the accepted conservation laws.

In 1932 Enrico Fermi renamed Pauli's "neutron" to neutrino as a word play on neutrone, the Italian name of the neutron [4], so as not to be confused with Chadwicks recently discovered particle. (Neutrone in Italian means big and neutral, and neutrino means small and neutral.) Three years later in 1934, Fermi published a very successful model of β-decay in which he unified Pauli's neutrino with P.A.M. Dirac's positron and Werner Heisenberg's neutron-proton model giving a solid theoretical basis to future experimental work [5, 6].

1.2 The First Experimental Observation of the Neutrino

In 1942 Wang Ganchang first proposed the use of beta-capture to experimentally detect neutrinos. In the July 20, 1956 issue of Science, Clyde Cowan, Frederick Reines, F. B. Harrison, H. W. Kruse, and A. D. McGuire published confirmation that they had detected the neutrino, a result that was rewarded almost forty years later with the 1995 Nobel Prize.

In this experiment, now known as the CowanReines neutrino experiment, antineutrinos created in a nuclear

reactor by beta decay reacted with protons producing neutrons and positrons:

$$\nu_e + \mathrm{p}^+ \longrightarrow \mathrm{n}^0 + \mathrm{e}^+ \tag{1.10}$$

Cowan and Reines used a nuclear reactor, as advised by Los Alamos physics division leader J.M.B. Kellogg as a source of a neutrino flux of 5×10^{13} neutrinos per second per cm^2; far higher than any attainable flux from other radioactive sources. The neutrinos then interacted, as shown in Eq. 1.10, with protons in a tank of water, creating neutrons and positrons. Each positron created a pair of gamma rays when it annihilated with an electron. The gamma rays were detected by placing a scintillator material in a tank of water, which gave off flashes of light in response to the gamma rays, and the flashes of light were in turn detected by photomultiplier tubes.

Detecting the positron-electron annihilation signal was not conclusive enough, so they devised a second layer of certainty via neutron detection done by placing cadmium chloride in the tank. Cadmium is a highly effective neutron absorber and gives off a gamma ray when it absorbs a neutron via the interaction shown in Eq. 1.11.

$$\mathrm{n} + {}^{108}\mathrm{Cd} \longrightarrow {}^{109\mathrm{m}}\mathrm{Cd} \longrightarrow {}^{109}\mathrm{Cd} + \gamma \tag{1.11}$$

This experimental setup was such that the gamma ray from the neutron-cadmium interaction would be detected 5 microseconds after the gamma ray from the positron-electron annihilation, giving the neutrino interaction a time coincidence based finger print.

Cowan and Reines initially performed the experiment at the Hanford Site, but later moved the experiment to the Savannah River Plant in Aiken, South Carolina where they had better shielding against cosmic rays. This shielded location was 11 m from the reactor and 12 m underground.

The Physical setup consisted of two tanks with a total of 200 L of water with 40 kg of dissolved $CdCl_2$. The two water tanks were then sandwiched between three scintillator layers which contained 110 five-inch (127 mm) photomultiplier tubes.

After months of data collection, they had accumulated data on about three neutrinos per hour in their detector. To be absolutely sure that they were seeing neutrino events from the detection scheme described above, they shut down the reactor to show that there was a difference in the number of detected events.

Their results were published in 1956 showing they had predicted a cross-section for the reaction to be $\sim 6 \times 10^{-44} cm^2$ while their measured cross-section was $6.3 \times 10^{-44} cm^2$. Although Clyde Cowan died in 1974, Frederick Reines was honored with the Nobel Prize in 1995 for his work on neutrino physics.

Neutrino Flavors

Subsequent experiments showed that there were not only a single type of neutrino but two other types, or flavors, one corresponding to each charged lepton - the electron, the muon and the tau.

In 1962 Leon M. Lederman, Melvin Schwartz and Jack Steinberger showed that more than one type

of neutrino exists by first detecting interactions of the muon neutrino (already hypothesised with the name neutretto) [7] which earned them the 1988 Nobel Prize in Physics. When the third type of lepton, the tau, was discovered in 1975 at the Stanford Linear Accelerator Center, it too was expected to have an associated neutrino (the tau neutrino). First evidence for this third neutrino type came from the observation of missing energy and momentum in tau decays analogous to the beta decay leading to the discovery of the neutrino. The first detection of tau neutrino interactions was announced in summer of 2000 by the DONUT collaboration at Fermilab [8], making it the latest particle of the Standard Model to have been directly observed; its existence had already been inferred by both theoretical consistency and experimental data from the Large ElectronPositron Collider.

1.3 Missing Neutrinos

As Neutrino experiments continued it was evident that the neutrino flux expected at detector sites did not match what was physically measured. This deficit was primarily evident from two sources of neutrino - solar neutrinos and atmospheric neutrino. This deficit, also observable in reactor based and accelerator based neutrino experiments, would provide the experimental evidence to substantiate the theoretical concept of neutrino oscillation.

1.3.1 The Solar Neutrino Problem

In the late 1960's, Ray Davis's and John N. Bahcall's Homestake Experiment was the first to measure the flux of neutrinos from the Sun and detect a deficit. The experiment used a chlorine-based detector. Many subsequent radiochemical and water Cerenkov detectors would confirm this deficit, including the Sudbury Neutrino Observatory.

The expected number of solar neutrinos had been computed based on the Standard Solar Model (SSM) which Bahcall had helped to establish and which gives a detailed account of the Sun's internal operation. The SSM predicts two main sources for solar neutrinos - the pp chain reaction [see Fig. 1.2a] and the CNO cycle [see Fig. 1.2b].

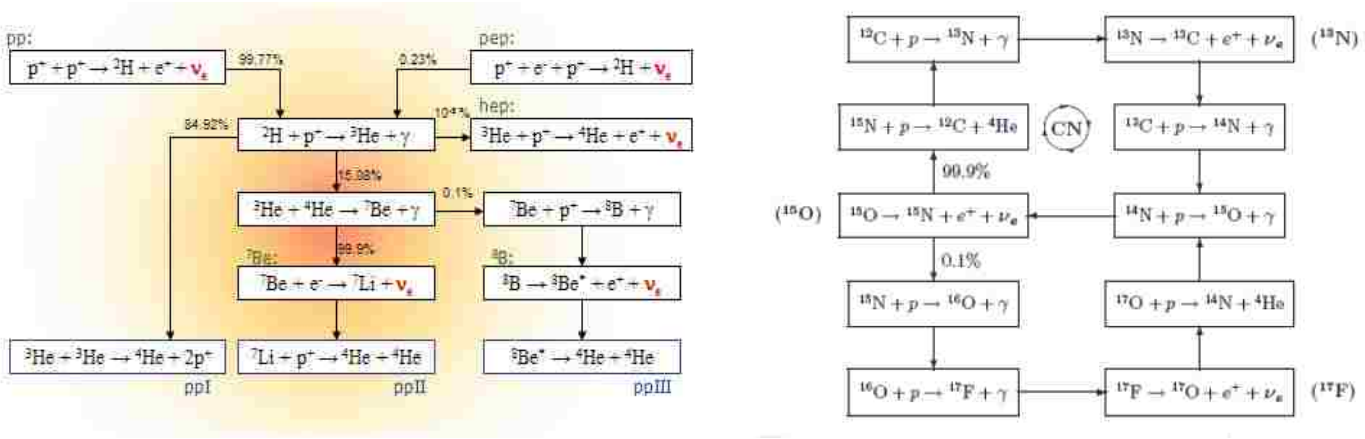

(a) (b)

Figure 1.2: The above diagrams show the chain of reactions responsible for the production of solar neutrinos. 1.2a shows the pp chain, while 1.2b shows the CNO cycle.

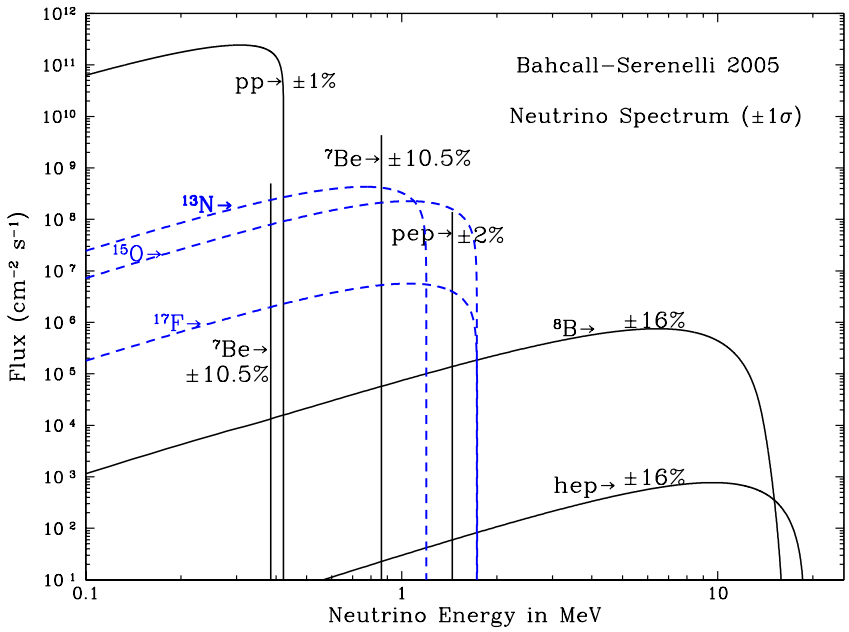

Figure 1.3: Neutrino flux at Earth predicted by the Standard Solar Model of 2005. The neutrinos produced in the pp chain are shown in black, neutrinos produced by the CNO cycle are shown in blue. The solar neutrino spectrum predicted by the BS05(OP) standard solar model. The neutrino fluxes from continuum sources are given in units of number $cm^2 s^1 MeV^1$ at one astronomical unit, and the line fluxes are given in number $cm^2 s^1$.

In 2002 Ray Davis and Masatoshi Koshiba won part of the Nobel Prize in Physics for experimental work that found the number of solar neutrinos was around a third of the number predicted by the Standard Solar Model [9].

Currently, the solar neutrino problem is believed to have resulted from an inadequate understanding of the properties of neutrinos. According to the Standard Model of particle physics, there are three different kinds of neutrinos: (1) electron neutrinos (which are the ones produced in the Sun and the ones detected by the above-mentioned experiments, in particular the chlorine-detector Homestake Mine experiment), (2) muon neutrinos, and (3) tau neutrinos.

In the 1970's, it was widely believed that neutrinos were massless and their types were invariant. However, in 1968 Pontecorvo proposed that if neutrinos had mass, then they could change from one type to another[10]. Thus, the "missing" solar neutrinos could be electron neutrinos which changed into other types along the way to Earth and therefore escaped detection.

The supernova 1987A produced an indication that neutrinos might have mass, because of the difference in time of arrival of the neutrinos detected at Kamiokande and IMB [11]. However, because very few neutrino events were detected it was difficult to draw any conclusions with certainty. In addition, whether neutrinos have mass or not could have been more definitively established had Kamiokande and IMB both had high precision timers which would have recorded how long it took the neutrino burst to travel through the Earth. If neutrinos were massless, they would travel at the speed of light; if they had mass, they would travel at velocities slightly less than that of light. Because the detectors were not intended for supernova neutrino detection, however, this was not done.

The convincing evidence for solar neutrino oscillation came in 2001 from the Sudbury Neutrino Observatory (SNO) in Canada. It detected all types of neutrinos coming from the Sun [12], and was able to distinguish between electron-neutrinos and the other two flavors (but could not distinguish the muon and tau flavours), by uniquely using heavy water as the detection medium. After extensive statistical analysis, it was found that about 35% of the arriving solar neutrinos are electron-neutrinos, with the others being muon- or tau-neutrinos [13]. The total number of detected neutrinos agrees quite well with the earlier predictions from nuclear physics, based on the fusion reactions inside the Sun.

1.3.2 Atmospheric Neutrinos

Solar Neutrinos are not the only natural source of neutrinos incident upon the Earth. Atmospheric neutrinos released in showers of cosmic rays also produce neutrinos detectable on Earth. When pions are released in the decay chains started by cosmic rays, the pions decay releasing neutrinos and muons which in turn decay releasing neutrinos and electrons:

$$\begin{aligned} &\pi^+ \rightarrow \mu^+ + \nu_\mu \\ &\mu^+ \rightarrow e^+ + \nu_e + \bar{\nu_\mu} \end{aligned} \tag{1.12}$$

or

$$\begin{aligned} &\pi^- \rightarrow \mu^- + \bar{\nu_\mu} \\ &\mu^- \rightarrow e^- + \bar{\nu_e} + \nu_\mu \end{aligned} \tag{1.13}$$

Large detectors such as IMB, MACRO, and Kamiokande II observed a deficit in the ratio of the flux of muon to electron flavor atmospheric neutrinos. The first strong evidence for neutrino oscillation in the

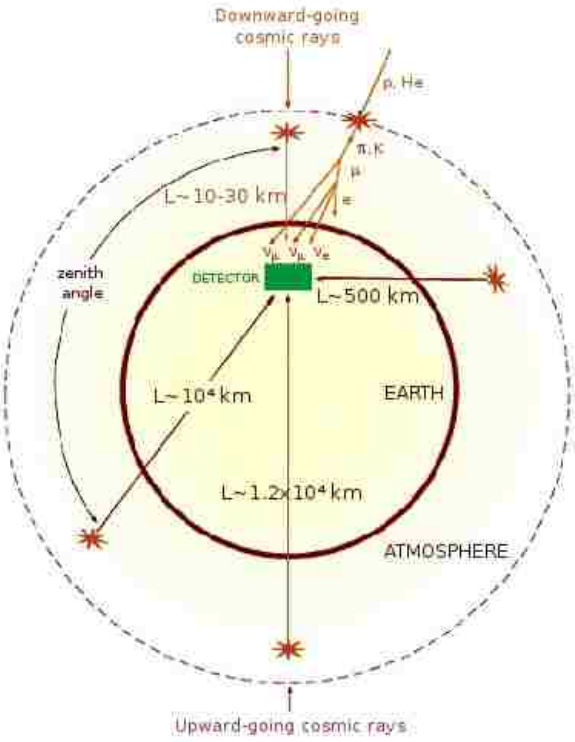

Figure 1.4: The above diagram shows the fundamental setup of the Super-Kamiokande experiment in Japan. Th goal of the experiment was to detect the flux of atmospheric neutrinos comparing the flux of those from overhead to the flux those traveling through the Earth.

atmospheric sector came in 1998 from the Super-Kamiokande collaboration in Japan [14]. It produced observations consistent with muon-neutrinos (produced in the upper atmosphere by cosmic rays as shown in Eq. 1.12) changing into tau-neutrinos. What was proved was that fewer neutrinos were detected coming through the Earth than could be detected coming directly above the detector [see Fig. 1.4]. Not only that, their observations only concerned muon neutrinos coming from the interaction of cosmic rays with the Earth's atmosphere. No tau neutrinos were observed at Super-Kamiokande.

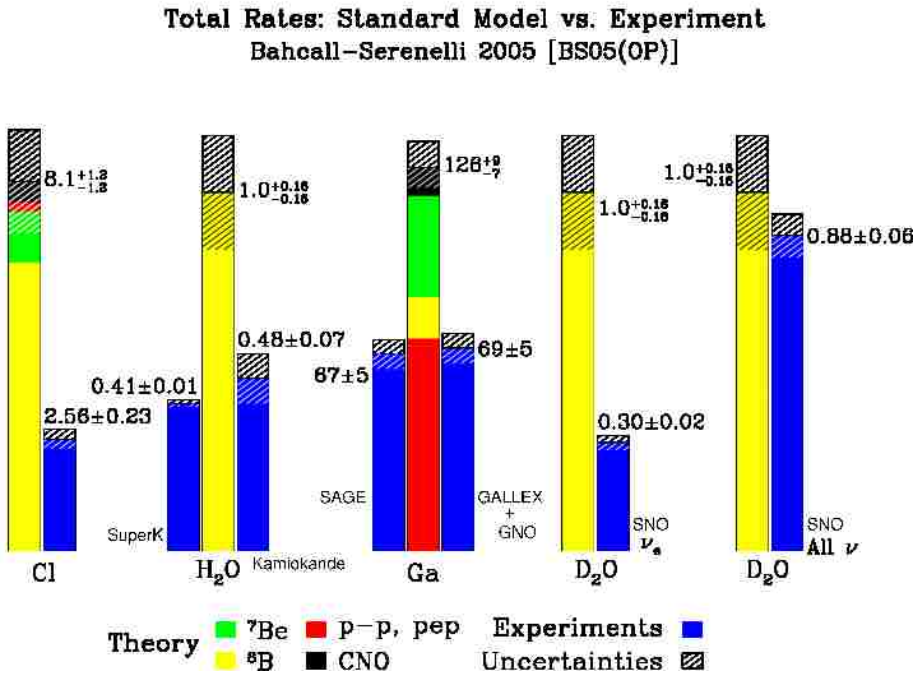

Figure 1.5: Theory versus experiment. The figure compares the predictions of the standard solar model plus the standard model of electroweak interactions with the measured rates in all solar neutrino experiments.

1.4 The Formalism of Neutrino Oscillations

Neutrino oscillation arises from a mixture between the flavor and mass eigenstates of neutrinos. That is, the three neutrino states that interact with the charged leptons in weak interactions are each a different superposition of the three neutrino states of definite mass. Neutrinos are created in weak decays and reactions in their flavor eigenstates. As a neutrino propagates through space, the quantum mechanical phases of the three mass states advance at slightly different rates due to the slight differences in the neutrino masses. This results in a changing mixture of mass states as the neutrino travels, but a different mixture of mass states corresponds to a different mixture of flavor states. So a neutrino born as, say, an electron neutrino will be some mixture of electron, mu, and tau neutrino after traveling some distance. Since the quantum mechanical phase advances in a periodic fashion, after some distance the state will nearly return to the original mixture, and the neutrino will be again mostly electron neutrino. The electron flavor content of the neutrino will then continue to oscillate as long as the quantum mechanical state maintains coherence. It is because the mass differences between the neutrinos are small that the coherence length for neutrino oscillation is so long, making this microscopic quantum effect observable over macroscopic distances.

1.4.1 The PMNS Matrix

The idea of neutrino oscillation was first put forward in 1957 by Bruno Pontecorvo, who proposed that neutrino-antineutrino transitions may occur in analogy with neutral kaon mixing [15]. Although such matter-antimatter oscillation has not been observed, this idea formed the conceptual foundation for the

quantitative theory of neutrino flavor oscillation, which was first developed by Maki, Nakagawa, and Sakata in 1962 [16] and further elaborated by Pontecorvo in 1967 [17]. One year later the solar neutrino deficit was first observed [18], and that was followed by the famous paper of Gribov and Pontecorvo published in 1969 titled "Neutrino astronomy and lepton charge" [10].

The unitary transformation relating the flavor and mass eigenbases can be written

$$|\nu_\alpha\rangle = \sum_i U_{\alpha i} \, |\nu_i\rangle \tag{1.14}$$

$$|\nu_i\rangle = \sum_\alpha U^*_{\alpha i} \, |\nu_\alpha\rangle \tag{1.15}$$

where the following are true:

1. $|\nu_\alpha\rangle$ is a neutrino with definite flavor with $\alpha =$ e (electron), μ (muon) or τ (tauon).
2. $|\nu_i\rangle$ is a neutrino with definite mass m_i with $i = 1, 2, 3$.
3. The asterisk (*) represents a complex conjugate. For antineutrinos, the complex conjugate should be dropped from the second equation, and added to the first.

$U_{\alpha i}$ represents the "Pontecorvo-Maki-Nakagawa-Sakata matrix" (also called the "PMNS matrix", "lepton mixing matrix", or sometimes simply the "MNS matrix"). It is the analogue of the Cabibbo-Kobayashi-Maskawa matrix, or CKM matrix, describing the analogous mixing of quarks. If this matrix were the identity matrix, then the flavor eigenstates would be the same as the mass eigenstates. However, experiment shows that it is not.

When the standard three neutrino theory is considered, the matrix is 3×3. If only two neutrinos are considered, a 2×2 matrix is used. [1] In the 3×3 form, it is given by [19]:

$$U = \begin{bmatrix} U_{e1} & U_{e2} & U_{e3} \\ U_{\mu 1} & U_{\mu 2} & U_{\mu 3} \\ U_{\tau 1} & U_{\tau 2} & U_{\tau 3} \end{bmatrix} \tag{1.16}$$

$$= \begin{bmatrix} 1 & 0 & 0 \\ 0 & c_{23} & s_{23} \\ 0 & -s_{23} & c_{23} \end{bmatrix} \begin{bmatrix} c_{13} & 0 & s_{13}e^{-i\delta} \\ 0 & 1 & 0 \\ -s_{13}e^{i\delta} & 0 & c_{13} \end{bmatrix} \begin{bmatrix} c_{12} & s_{12} & 0 \\ -s_{12} & c_{12} & 0 \\ 0 & 0 & 1 \end{bmatrix} \begin{bmatrix} e^{i\alpha_1/2} & 0 & 0 \\ 0 & e^{i\alpha_2/2} & 0 \\ 0 & 0 & 1 \end{bmatrix} \tag{1.17}$$

$$= \begin{bmatrix} c_{12}c_{13} & s_{12}c_{13} & s_{13}e^{-i\delta} \\ -s_{12}c_{23} - c_{12}s_{23}s_{13}e^{i\delta} & c_{12}c_{23} - s_{12}s_{23}s_{13}e^{i\delta} & s_{23}c_{13} \\ s_{12}s_{23} - c_{12}c_{23}s_{13}e^{i\delta} & -c_{12}s_{23} - s_{12}c_{23}s_{13}e^{i\delta} & c_{23}c_{13} \end{bmatrix} \begin{bmatrix} e^{i\alpha_1/2} & 0 & 0 \\ 0 & e^{i\alpha_2/2} & 0 \\ 0 & 0 & 1 \end{bmatrix} \tag{1.18}$$

[1] If one or more sterile neutrinos are added it is 4×4 or larger. The topic of sterile neutrinos are not discussed herein as they beyond the scope of this paper.

where $c_{ij} = \cos\theta_{ij}$ and $s_{ij} = \sin\theta_{ij}$. The phase factors α_1 and α_2 are physically meaningful only if neutrinos are Majorana particles - i.e. if the neutrino is identical to the antineutrino - and do not enter into oscillation phenomena regardless. If neutrinoless double beta decay ($0\nu\beta\beta$) occurs indicating the neutrino is indeed a Majorana particle, then these factors influence its rate. The phase factor δ is non-zero only if neutrino oscillation violates CP symmetry. Although there is some expectation for this phenomena it has not yet been observed experimentally. If experiment shows this 3×3 matrix to be not unitary, a sterile neutrino or some other new physics is required.

If neutrinos are Dirac particles then the Majorana phases vanish and we can disregard the matrix furthest to the right hand side of Eq. 1.17. We will make this assumption from now on, as the Majorana phases do not affect neutrino oscillation process. Thus, Eq. 1.17 becomes:

$$U = \begin{bmatrix} 1 & 0 & 0 \\ 0 & c_{23} & s_{23} \\ 0 & -s_{23} & c_{23} \end{bmatrix} \begin{bmatrix} c_{13} & 0 & s_{13}e^{-i\delta} \\ 0 & 1 & 0 \\ -s_{13}e^{i\delta} & 0 & c_{13} \end{bmatrix} \begin{bmatrix} c_{12} & s_{12} & 0 \\ -s_{12} & c_{12} & 0 \\ 0 & 0 & 1 \end{bmatrix} \tag{1.19}$$

1.4.2 Propagation & Interference

Since $|\nu_i\rangle$ are mass eigenstates, then their propagation can be described by plane wave solutions of the form

$$|\nu_i(t)\rangle = e^{-i(E_i t - \vec{p}_i \cdot \vec{x})}|\nu_i(0)\rangle \tag{1.20}$$

where the quantities are expressed in natural units, i.e. $c = 1$ and $\hbar = 1$. The term E_i represents the energy of the mass-eigenstate i and t is the time from the start of the propagation. The variable $\vec{p}_i$ represents the three-dimensional momentum and $\vec{x}$ is the current position of the particle relative to its starting position.

In the ultrarelativistic limit, $|\vec{p}_i| = p_i \gg m_i$, and we can approximate the energy as

$$E_i = \sqrt{p_i^2 + m_i^2} \simeq p_i + \frac{m_i^2}{2p_i} \approx E + \frac{m_i^2}{2E} \tag{1.21}$$

This limit applies to all practical (currently observed) neutrinos, since their masses are less than 1 eV and their energies are at least 1 MeV, so the Lorentz factor γ is greater than 10^6 in all cases. Using also $t \approx L$, where L is the distance traveled and also dropping the phase factors, the wavefunction becomes:

$$|\nu_i(L)\rangle = e^{-im_i^2 L/2E}|\nu_i(0)\rangle \tag{1.22}$$

Eigenstates with different masses propagate at different speeds, i.e. the heavier ones lag behind while the lighter ones pull ahead. Since the mass eigenstates are combinations of flavor eigenstates, this difference in speed causes interference between the corresponding flavor components of each mass eigenstate. Constructive interference causes it to be possible to observe a neutrino created with a given flavor to change its

flavor during its propagation. The probability that a neutrino originally of flavor α will later be observed as having flavor β is

$$\begin{aligned} P_{\alpha\to\beta} = \delta_{\alpha\beta} \quad &- \quad 4\sum_{i>j} \mathrm{Re}(U^*_{\alpha i}U_{\beta i}U_{\alpha j}U^*_{\beta j}) \sin^2(\tfrac{\Delta m^2_{ij}L}{4E}) \\ &+ \quad k\cdot 2\sum_{i>j} \mathrm{Im}(U^*_{\alpha i}U_{\beta i}U_{\alpha j}U^*_{\beta j}) \sin(\tfrac{\Delta m^2_{ij}L}{2E}) \end{aligned} \tag{1.23}$$

where $\Delta m^2_{ij} \equiv m^2_i - m^2_j$ and $k = 1$ for neutrinos and $k = -1$ for antineutrinos. This is more conveniently written as

$$P_{\alpha\to\beta} = |\langle\nu_\beta|\nu_\alpha(t)\rangle|^2 = \left|\sum_i U^*_{\alpha i}U_{\beta i}e^{-im^2_i L/2E}\right|^2 \tag{1.24}$$

The phase that is responsible for oscillation is often written as (with c and $\hbar$ restored)

$$\frac{\Delta m^2\, c^3\, L}{4\hbar E} = \frac{\mathrm{GeV\,fm}}{4\hbar c} \times \frac{\Delta m^2}{\mathrm{eV}^2}\frac{L}{\mathrm{km}}\frac{\mathrm{GeV}}{E} \approx 1.267 \times \frac{\Delta m^2}{\mathrm{eV}^2}\frac{L}{\mathrm{km}}\frac{\mathrm{GeV}}{E} \tag{1.25}$$

where 1.267 is unitless. In this form, it is convenient to plug in the oscillation parameters since the mass differences, Δm^2_{ij}, are known to be on the order of $1 \times 10^{-4} eV^2$, oscillation distances, L, in modern experiments are on the order of kilometers and neutrino energies, E, in modern experiments are typically on order of MeV or GeV.

At this point it is clear that for the three flavor Dirac case, mixing is determined by seven parameters: three mixing angles θ_{12}, θ_{13}, and θ_{23}, three mass splittings Δm^2_{12}, Δm^2_{13}, and Δm^2_{23} (only two of which are independent), and one phase δ.

Experimentally, the mass difference between m_1 and m_2 is much smaller than the difference between these and m_3, so the approximate parametrization (Δm^2, ΔM^2) is often used, where $\Delta m^2 = \Delta m^2_{12}$ and $\Delta M^2 \simeq \Delta m^2_{13} \simeq \Delta m^2_{23}$. Vacuum oscillations cannot determine the sign of the mass splittings; these can be measured using matter effects (discussed in Section 1.2.4). Δm^2 is known to be positive from solar neutrino data, but the sign of ΔM^2 is presently unknown. The case where m_3 is the most massive state is referred to as the normal mass hierarchy, and the case where it is least massive as the inverted mass hierarchy, as shown in Figure 1.6.

Additionally, it should be noted that the right most matrix in Eq. 1.19 is dependent only on $\theta_{12} \equiv \theta_{sol}$. Solar neutrino experiments combined with KamLAND have measured the so-called solar parameters $\sin^2\theta_{sol}$ and $\Delta m^2_{sol} \equiv \Delta m^2_{12}$.

In like manner, the left most matrix in Eq. 1.19 is dependent only on $\theta_{23} \equiv \theta_{atm}$. Atmospheric neutrino experiments such as Super-Kamiokande together with the K2K and MINOS long baseline accelerator neutrino experiment have determined the so-called atmospheric parameters $\sin^2\theta_{atm}$ and $\Delta m^2_{atm} \equiv \Delta m^2_{23}$.

As mentioned above, Δm^2_{13} is related to solar neutrino experiments, as well as long baseline reactor

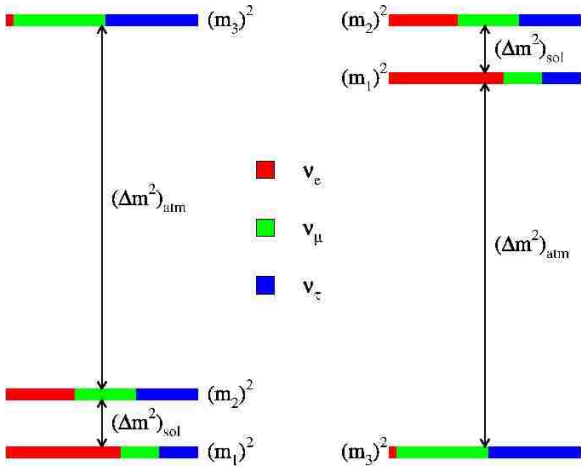

Figure 1.6: This diagram shows the mass states and their approximate flavor composition in the normal (left) and inverted (right) mass hierarchies, where the $mass^2$ increases from bottom to top. The ν_e component of ν_3 is small and may be zero. The size of Δm^2 relative to ΔM^2 is exaggerated, and the absolute mass values are unknown.

experiments, i.e. experiments with large L/E and where $\nu_e \to \nu_\mu, \nu_\tau$ transitions dominate. Whereas, Δm^2_{23} is related to atmospheric neutrino experiments, as well as long baseline accelerator neutrino experiments, i.e. experiments with small L/E and where $\nu_\mu \to \nu_\tau$ transitions dominate. The fact that the atmospheric and solar regimes can be studied separately, or decoupled, is in part due to the small size of θ_{13}, and this decoupling allows a first approximation to be made via two flavor mixing.

1.4.3 Two Flavor Mixing

The above formula is correct for any number of neutrino generations. Writing it explicitly in terms of mixing angles is extremely cumbersome if there are more than two neutrinos that participate in mixing. Fortunately, there are several cases in which only two neutrinos participate significantly. In this case, it is sufficient to consider the mixing matrix

$$U = \begin{pmatrix} \cos\theta & \sin\theta \\ -\sin\theta & \cos\theta \end{pmatrix} \tag{1.26}$$

Then the probability of a neutrino changing its flavor, also known as neutrino appearance, in natural units is

$$P_{\alpha\to\beta,\alpha\neq\beta} = \sin^2(2\theta)\,\sin^2\left(\frac{\Delta m^2 L}{4E}\right) \tag{1.27}$$

Or, using SI units and the convention introduced above

$$P_{\alpha\to\beta,\alpha\neq\beta} = \sin^2(2\theta)\,\sin^2\left(1.267\frac{\Delta m^2 L}{E}\frac{\text{GeV}}{\text{eV}^2\,\text{km}}\right) \tag{1.28}$$

Whereas the probability of a neutrino remaining the same flavor, known as neutrino disappearance, in natural units is

$$P_{\alpha\to\alpha} = 1 - \sin^2(2\theta)\,\sin^2\left(\frac{\Delta m^2 L}{4E}\right) \tag{1.29}$$

As above, where Eq. 1.27 is converted to SI units yielding Eq. 1.28, Eq. 1.29 can likewise be converted to SI units giving

$$P_{\alpha\to\alpha} = 1 - \sin^2(2\theta)\,\sin^2\left(1.267\frac{\Delta m^2 L}{E}\frac{\mathrm{GeV}}{\mathrm{eV}^2\,\mathrm{km}}\right) \tag{1.30}$$

This formula is often appropriate for discussing the transition $\nu_\mu \leftrightarrow \nu_\tau$ in atmospheric mixing, since the electron neutrino plays almost no role in this case. It is also appropriate for the solar case of $\nu_e \leftrightarrow \nu_x$, where ν_x is a superposition of ν_μ and ν_τ. These approximations are possible because the mixing angle θ_{13} is very small and because the mass difference between m_1 and m_2 is much smaller than the difference between these and m_3.

1.4.4 Oscillation Channels Relevant to T2K

T2Ks main goal is to measure θ_{13} via the search for ν_e appearance in a ν_μ beam. In addition to θ_{13}, θ_{23} and Δm^2_{23} will also be measured. In a later stage of the experiment δ, the parameter related to CP violation, can be measured but only under the condition that $\theta_{13} \neq 0$.

Most of the PMNS matrix parameters have been measured, except for the mixing angle $\theta 13$ and the CP-violation phase δ. T2Ks main goal of measuring $\theta 13$ will be achieved through the search for ν_e appearance in a ν_μ beam. Assuming that $\Delta m^2_{23} \sim \Delta m^2_{13}$, the probability of ν_e appearance from a ν_μ beam is:

$$\begin{aligned} P(\nu_\mu \to \nu_e) = &\sin^2(\theta_{23})\sin^2(2\theta_{13})\sin^2(1.27\Delta m^2_{23}L/E_\nu) \\ &+ \cos^2(\theta_{23})\sin^2(2\theta_{13})\sin^2(1.27\Delta m^2_{12}L/E_\nu) \\ &- J\sin(\delta)\sin(1.27\Delta m^2_{23}L/E_\nu) \\ &+ J\cos(\delta)\cos(1.27\Delta m^2_{23}L/E_\nu) \end{aligned} \tag{1.31}$$

where

$$J = \cos(\theta_{13})\sin(2\theta_{12})\sin(2\theta_{13})\sin(2\theta_{23})\sin(1.27\Delta m^2_{23}L/E_\nu)\sin(1.27\Delta m^2_{12}L/E_\nu)$$

Furthermore, if we assume that $\delta = 0$ and if we neglect matter effects, as described by the MSW effect[2],

[2]Not discussed herein as it is beyond the scope of this paper.

then the oscillation probabilities can be simplified into:

$$P(\nu_\mu \to \nu_e) = \sin^2(2\theta_{13}) \sin^2(\theta_{23}) \sin^2(1.27\Delta m^2_{13} L/E_\nu) \tag{1.32}$$

$$P(\nu_\mu \to \nu_\mu) = 1 - \cos^4(\theta_{13}) \sin^2(2\theta_{23}) \sin^2(1.27\Delta m^2_{23} L/E_\nu) \tag{1.33}$$

Although the exact value of θ_{13} is not yet known, the existing upper limit on it shows that the angle is smaller than 11°. Therefore, the central matrix in Eq. **??** is often replaced by the identity matrix when looking for the solar neutrino oscillations (dominated by θ_{12} and Δm^2_{12}) or the atmospheric neutrino oscillations (dominated by θ_{23} and Δm^2_{23}). By applying this approximation on Eq. 1.32 and Eq. 1.33, we obtain that $P(\nu_\mu \to \nu_e) \cong 0$ and

$$\begin{aligned} P(\nu_\mu \to \nu_\mu) &= 1 - \sin^2(2\theta_{23}) \sin^2(1.27\Delta m^2_{23} L/E_\nu) \\ &= 1 - P_{2flavor}(\nu_\mu \to \nu_\tau) \end{aligned} \tag{1.34}$$

where $P_{2flavor}(\nu_\mu \to \nu_\tau)$ is the oscillation probability computed considering only two neutrino flavors, ν_μ and ν_τ. Evidently, the two-flavor approach is not merely a simplification, it is in fact a good approximation of the three-flavor mixing when we consider the actual values of the mixing parameters. This approximation has been used in the solar and reactor neutrino experiments (SNO, KamLAND), as well as in the atmospheric neutrino and long baseline neutrino experiments.

Chapter 2

The Tokai to Kamiokande (T2K) Long Baseline Neutrino Experiment: An Overview

Figure 2.1: A bird's eye view of the layout of the T2K experiment.

2.1 General Overview of the T2K Experiment

The T2K (Tokai-to-Kamioka) experiment is a long baseline neutrino oscillation experiment designed to probe the mixing of the muon neutrino with other species and shed light on the neutrino mass scale. It is the first long baseline neutrino oscillation experiment designed to explicitly look for the electron neutrino appearance from the muon neutrino, and in so doing measure θ_{13}.

T2Ks physics goals include the measurement of the neutrino oscillation parameters with precision of $\delta(\Delta m^2_{23}) \sim 10^4 eV^2$ and $\delta(\sin^2 2\theta_{23}) \sim 0.01$ via ν_μ disappearance studies, resulting in a factor of nearly 20 times better sensitivity than compared to the limit on θ_{13} from the CHOOZ experiment through the search for $\nu_\mu \rightarrow \nu_e$ appearance ($\sin^2 2\theta_{\mu e} \simeq \frac{1}{2}\sin^2 2\theta_{13} > 0.004$ at 90% CL for CP violating phase $\delta = 0$). In addition to neutrino oscillation studies, the T2K neutrino beam (with $E_\nu \sim 1GeV$) will enable a multifaceted fixed-target physics program of neutrino interaction studies at energies covering the transition between the resonance production and deep inelastic scattering regimes.

T2K uses Super-Kamiokande as the far detector to measure neutrino rates at a distance of 295 km from the accelerator, and near detectors to sample the beam just after production. The experiment includes a neutrino beamline and a near detectorcomplex at 280 m (ND280), both of which were newly constructed. Super-Kamiokande was upgraded and restored to 40% photocathode coverage (the same as the original Super-Kamiokande detector) with new photomultiplier tubes in 2005-2006, following the accident of 2001. Fig. 2.2 shows a schematic layout of the T2K experiment as a whole.

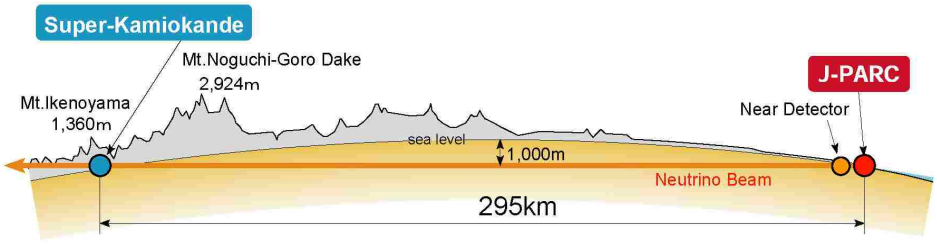

Figure 2.2: The above diagram shows the neutrino beam's 295 km trip from the J-PARC facility through the near detectors, which characterize the initial properties of the beam, and on to Super-K - the far detector.

T2K adopts the off-axis method to generate the narrow band neutrino beam using the new MW-class proton synchrotron at J-PARC4. In this method the neutrino beam is purposely directed at an angle with respect to the baseline connecting the proton target and the far detector, Super-Kamiokande. The off-axis angle is set at 2.5° so that the narrow-band muon neutrino beam generated toward the far detector has a peak energy at $\sim 0.6GeV$, which maximizes the effect of the neutrino oscillation at 295 km and minimizes the background to electron-neutrino appearance detection [see Fig. 2.4]. The angle can be reduced to 2.0°, allowing variation of the peak neutrino energy, if necessary.

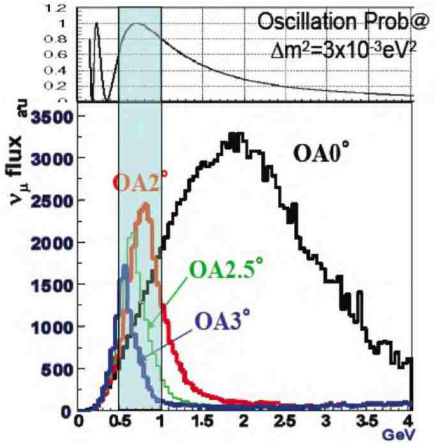

Figure 2.3: The above plot shows that ν_μ oscillation probability is maximized at a peak beam energy of $\sim 0.6Gev$ when L = 295 km and the beam is at an off-axis angle of 2.5°.

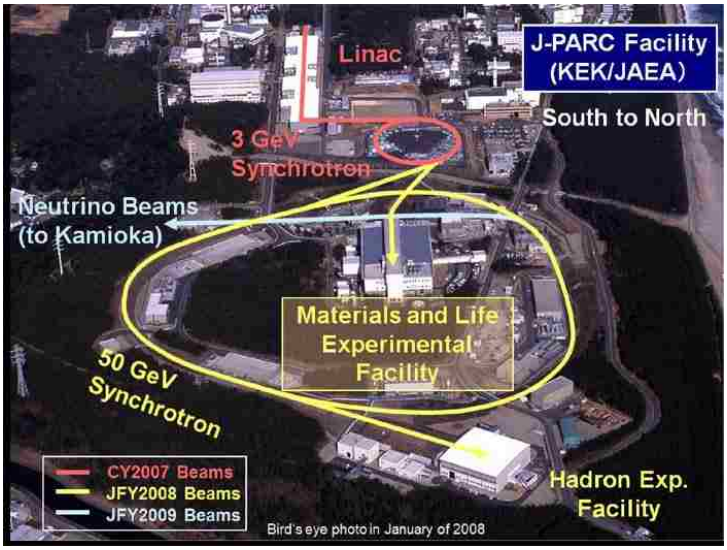

Figure 2.4: An overhead view of the J-PARC facility with the main parts of the accelerator complex identified.

2.2 The J-PARC Accelerator Complex

J-PARC, which was newly constructed at Tokai, Ibaraki prefecture, consists of the following three accelerators:

1. A linear accelerator (LINAC).
2. A rapid-cycling synchrotron (RCS).
3. The main ring (MR) synchrotron.

An H^- beam is accelerated up to 400 MeV (181 MeV at present) by the LINAC, and is converted to an H^+ beam by charge-stripping foils at the RCS injection. The beam is then accelerated up to 3 GeV by the RCS with a 25 Hz cycle. The RCS has a harmonic number of two, and there are two bunches in a cycle. Roughly 5% of these bunches are supplied to the MR. The remaining bunches are supplied to the muon and neutron beamline, part of the Material and Life Science Facility. The proton beam injected into the MR is accelerated up to 30 GeV. The MR has a harmonic number of nine, and the number of bunches in the MR is eight (six before June 2010). The MR has two extraction points: the first is the slow extraction for the hadron beamline while the other is the fast extraction for the neutrino beamline.

Via the fast extraction mode, the eight circulating proton bunches are extracted within a single turn by a set of five kicker magnets. The time structure of the extracted proton beam is key to discriminating various backgrounds, including cosmic rays, in the various neutrino detectors. The various parameters of the MR for the fast extraction are listed in Tab. 2.1.

Table 2.1: The above table displays the various parameters of the MR for fast extraction. [1]

Circumference	1567 m
Beam power	$\sim$ 750 kW
Beam kinetic energy	30 GeV
Beam intensity	$\sim 3 \times 10^{14}$ p/spill
Spill cycle	$\sim$ 0.5 Hz
Number of bunches	8/spill
RF frequency	$1.67 - 1.72$ MHz
Spill width	$\sim 5\mu$sec

2.3 The Neutrino Beam

As noted above, each proton beam spill consists of eight proton bunches extracted from the MR to the T2K neutrino beamline, which in turn produces the neutrino beam. The neutrino beamline is composed of two sequential sections: the primary and secondary beamlines. In the primary beamline, the extracted proton beam is transported to point toward Kamioka. In the secondary beamline, the proton beam strikes a target to produce secondary pions, which are subsequently focused by magnetic horns and decay into neutrinos. Schematics of both the primary and secondary neutrino beamlines are shown in Fig. 2.5. An overview of the two beamline sections is given in the following paragraphs. The neutrino beamline is designed so that the neutrino energy spectrum at Super-Kamiokande can be tuned by changing the off-axis angle down to a minimum of $\sim 2.0^\circ$, from the current (maximum) angle of $\sim 2.5^\circ$. Precise measurements of the baseline distance and off-axis angle were determined by a GPS survey.

2.3.1 The Primary Beamline

The primary beamline consists of the preparation section (54 m long), the arc section (147 m), and the final focusing section (37 m). In the preparation section, the extracted proton beam is tuned with a series of eleven normal conducting magnets (four steering, two dipole and five quadrupole magnets) so that the beam can be accepted by the arc section. In the arc section, the beam is bent toward the direction of Kamioka by 80.7°, with a 104 m radius of curvature, using 14 doublets of superconducting combined function magnets (SCFMs). There are also three pairs of horizontal and vertical superconducting steering magnets to correct the beam orbit. In the final focusing section, ten normal conducting magnets (four steering, two dipole and four quadrupole magnets) guide and focus the beam onto the carbon target, while directing the beam downward by 3.637° with respect to the horizontal.

A well-tuned proton beam is essential for stable neutrino beam production, and to minimize beam loss in order to achieve high-power beam operation. Therefore, the intensity, position, profile and loss of the proton beam in the primary sections are precisely monitored by five current transformers (CTs), 21 electrostatic monitors (ESMs), 19 segmented secondary emission monitors (SSEMs) and 50 beam loss monitors (BLMs), respectively.

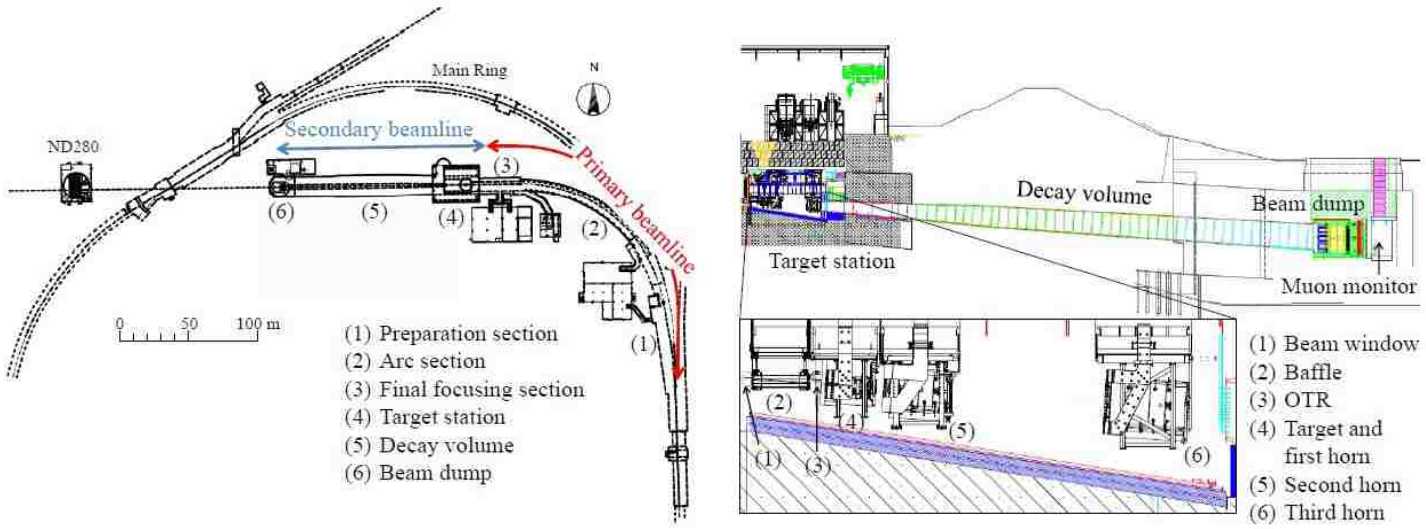

(a) (b)

Figure 2.5: The above diagrams are of the (a) primary beamline and the (b) secondary beamline.

2.3.2 The Secondary Beamline

The secondary beam starts where the proton beam collides onto the target, a 91.4 cm long × 2.6 cm diameter graphite rod. Prior to colliding onto the target, the proton beam is monitored by the Optical Transition Radiation (OTR) detector. The protons interact with the helium-cooled graphite target, primarily producing pions along with a smaller fraction of kaons. Since only the positively charged particles decay to produce the ν_μ required for the neutrino beam, then it is desirable to remove the negatively charged particles. This is achieved by passing the beam through three magnetic horns, which focus the positive particles, while simultaneously removing the negative particles. Each horn consists of two concentric aluminum cylinders, carrying a large electric current. The magnetic field produced inside the horn is circular and diminishes towards the center, thus bending any positive particles on the edges back in towards the center, while bending the negative particles outwards.

After passing through the horns, any remaining mesons will enter the decay volume. This volume, which is filled with inert helium gas held at a pressure of 1 atm, is 110 m long, and the cross-section starts at 2.2 m (W) × 2.8 m (H), increasing to 3.0 m × 4.6 m at the far end. Since a large number of particles will will strike the walls of the decay volume, they are constructed from iron plates and the entire volume is surrounded by 6 m of concrete. Additionally, since the particles carry a lot of energy water cooling channels have been built into the walls and are used to maintain the temperature in the decay volume.

Once inside the decay volume, the mesons decay by the following mechanisms:

$$\pi^+ \to \mu^+ + \nu_\mu \tag{2.1}$$
$$K^+ \to \mu^+ + \nu_\mu \tag{2.2}$$
$$K^+ \to e^+ + \nu_\mu + \pi^0 \tag{2.3}$$
$$K^0_L \to e^+ + \nu_\mu + \pi^- \tag{2.4}$$
$$\mu^+ \to e^+ + \nu_e + \bar{\nu_\mu} \tag{2.5}$$

where the muons in Eq. 2.5 derives from the primary pion or kaon decays. As it shows, a μ^+ would subsequently decay into a $\bar{\nu_\mu}$, a e^+, and aν_e contaminating the neutrino beam; the length of the decay volume has therefore been tuned to maximize pion decays while minimizing muon decays.

After decaying, the beam reaches the beam dump where the remaining mesons and low energy muons are removed leaving only muons with an energy greater than ~ 5 GeV and neutrinos to pass through the beam dump. The muons are detected by a downstream muon monitor (MUMON) to characterize the neutrino beam stability, intensity, and direction on a bunch-by-bunch basis.

2.4 Super-K: The Far Detector

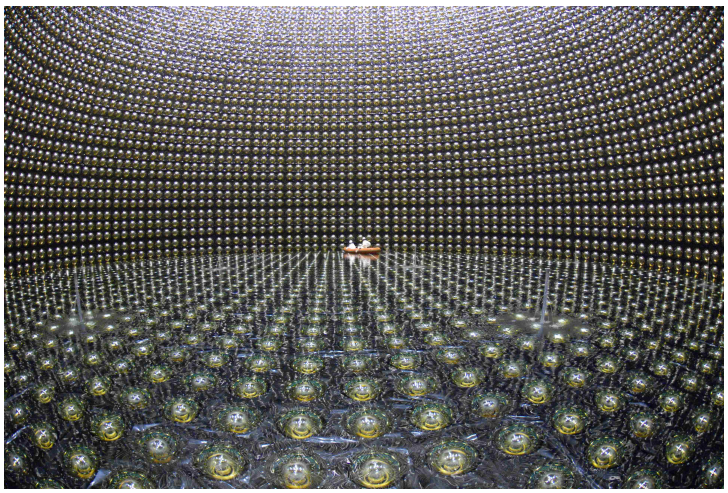

Figure 2.6: A view of the interior Super-Kamiokande filled with pure water. ©Kamioka Observatory, ICRR, The University of Tokyo

Super-Kamiokande, or Super-K [see Fig. 2.6), the largest water Cherenkov detector in the world, serves as the T2K far detector and is located at 295 km from the target. It was built within a 1 km deep mine at Kamioka (2.7 km water equivalent) and has been taking data since 1996. Super-K has produced a large number of important results for neutrino physics and currently has set the most stringent limit on proton lifetime. Super-K has been used in several experiments such as the eponymous Super-K experiment, which experimentally demonstrated the oscillations of neutrinos in the atmospheric sector , and K2K, the first long baseline neutrino oscillation experiment that studied the $\nu_\mu \to \nu_e$ oscillation with a ν_μ beam produced at KEK.

Super-K consists of a cylindrical tank of 41.4 m height and 39.3 m diameter filled with 50 ktons of pure water [see Fig. 2.7]. This volume is divided into two sub-volumes, the inner detector which contains 32 ktons of water whose walls are covered by 11,146 inward facing 50 cm diameter photo-multipliers (PMT) (40%surface coverage), and the outer detector surrounding the inner detector, instrumented with 1885 outward facing PMTs. The outer detector serves as an active veto and a radioactivity shield. An accident in November 2001 caused the loss of 60% of the PMTs, where the period before the accident is known as SK-I phase. SK was up and running again from December 2002 until the Fall of 2005 (SK-II phase) with half of its PMTs redistributed evenly over the whole surface. Between fall 2005 and spring 2006, SK was refitted with acrylic reinforced PMTs to prevent damage from chain reactions like the one that had caused major damage years prior. Data taking resumed in June 2006 (SK-III phase). Since September 2009, SK has run with an upgraded PMT readout electronics setup (SK-IV phase) and T2K is the first experiment using this enhanced setup.

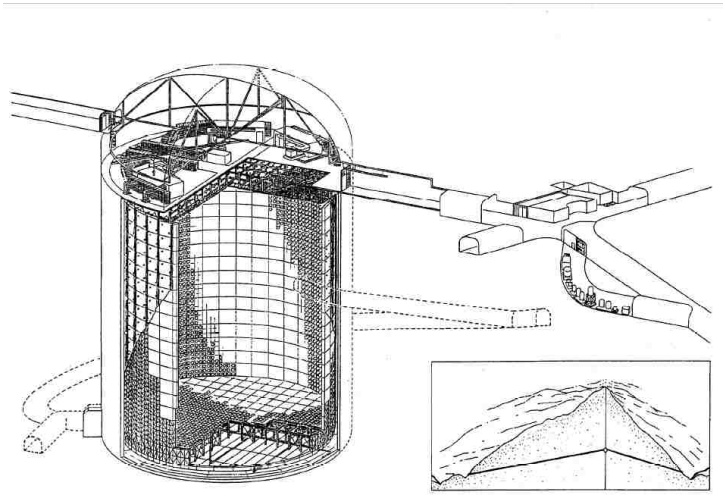

Figure 2.7: A drawing of the Super-Kamiokande detector, showing the tank, the electronics huts and water purification systems at the top of the tank, and the detector's position in Mt. Ikenoyama. ©Kamioka Observatory, ICRR, The University of Tokyo

The depth at which Super-Kamiokande is buried reduces the cosmic ray flux by five orders of magnitude with respect to the Earth's surface. Since SK has been used in several experiments, its behavior is well understood. The energy scale is well known, and the software for modeling events in the detector matches calibration samples as well.

Charged particles produced by neutrino interactions are detected by the Cherenkov light cone they produce as they cross the water when their energy is above the threshold. Super-K can easily distinguish the light rings produced by muons from the ones produced by electrons. As it can be seen in Fig. 2.8, muon-like rings have neat edges while electron-like rings have blurry edges due to electron scattering in water. The misidentification between electrons and muons is estimated to be $\sim$2% in the sub-GeV energy range.

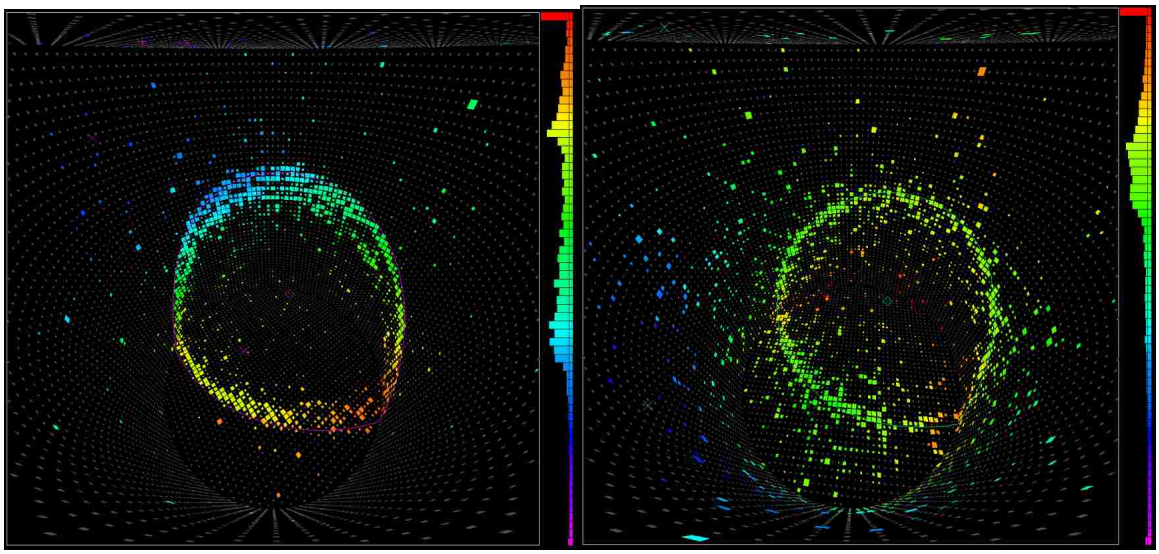

(a) (b)

Figure 2.8: Shown in 2.8a is a muon event whereas 2.8b shows an electron event in Super-K. The color scale indicates PMT hit times.

2.5 The Near Detector

The near detector complex consists of two detectors: the on-axis detector known as INGRID and the off-axis detector known as ND280 (Near Detector at 280m). Herein we focus on the ND280 detector [see Fig. 2.9a] as it contains the sub-detector which is the focus of this paper. The ND280 characterizes the neutrino beam before oscillation by measuring various quantities such as beam flux, composition, direction, neutrino energy spectra, and cross sections.

The detector is placed within the refurbished magnet from the UA1 experiment which provides a 0.2 T magnetic field. The ND280, while housed in the same pit as INGRID, is located on the on the first floor.

The off-axis ND280 is composed by a subset of different detector types: an upstream π^0 detector (P0D) and a tracker, surrounded by an electromagnetic calorimeter (downstream and barrel ECAL) and side muon range detectors (SMRD) embedded within the magnet yoke 2.9.All parts but the barrel electromagnetic calorimeter were installed and commissioned at the end of 2009, and took data for the first T2K run which was from January to June 2010. The magnet was operational and had been field mapped. The barrel electromagnetic calorimeter was installed during summer 2010 and started taking data at the end of 2010. The results presented in this thesis use the data from the first T2K run, i.e. before the barrel-ECAL installation.

2.5.1 P0D: The Pi-Zero Detector

The ND280's P0D sub-detector is located upstream of the other sub-detectors. It is designed to detect the γs from π^0s produced by ν_μ-NC (neutral current) interactions, and hence measure the cross-section for NC-π^0 production. It consists of three sections known as "Super P0Dules" - a main fiducial volume in the

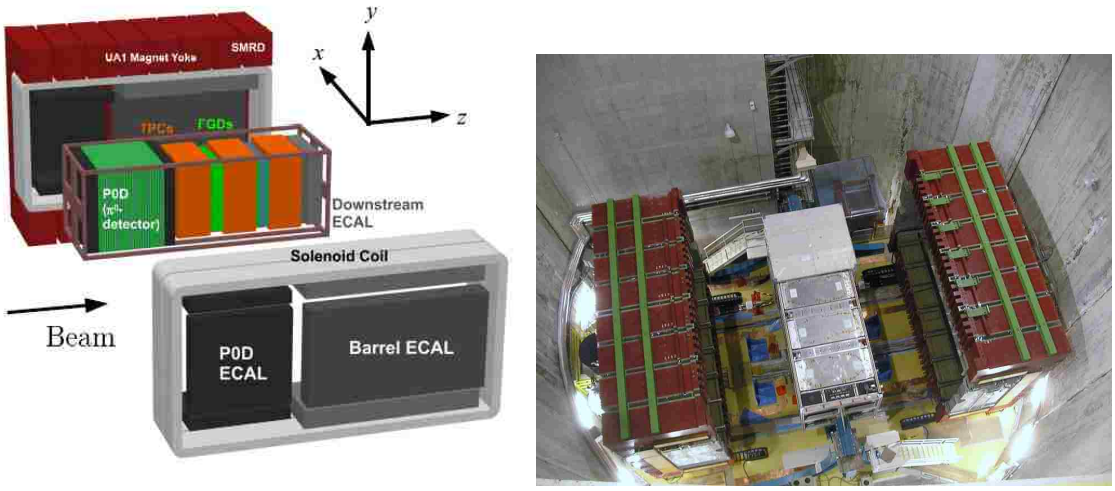

(a) (b)

Figure 2.9: [2.9a above left] A cutaway view of the ND280 detector with the various sub-detectors labeled. Shown are the left half of the magnetic yoke and coil, as well as the inner sub-detectors. Missing is the right half of the magnet. [2.9b above right] A photo of the ND280 detector located in the pit where it is installed; the magnetic yoke is open reveling the inner sub-detectors.

center, with modules optimized for calorimetry upstream and downstream. All modules are instrumented with triangular scintillator bars (33 mm base, 17 mm height, 2.14 m long), with two perpendicular layers glued together to give both X and Y information. Where the orthonormal geometry for the ND280, inclusive of all sub-detectors, has been defined such that, while facing in the direction the neutrino beam is traveling, the neutrino beam itself defines the +Z-axis as it travels from east to west, the +X-axis points to the left (or south), and hence the +Y-axis points upward. The central module has cavities between every second X-Y block, which can be filled with water, and also thin lead sheets between the X and Y layers to convert photons. The calorimeter modules contain no water cavities, and have thicker lead to ensure EM shower containment. The mass of the fiducial volume of the detector is 5.1 tonnes, of which 2 tonnes is water.

π^0s in the P0D are identified by locating a pair of showers which can be extrapolate back to a common vertex, while also having an invariant mass near the pion mass. This analysis relies on good tracking and energy resolution. The cross-section on water, which is important to reduce systematics on the ν_e appearance measurement at Super-K, is extracted by comparing the rates with the water cavities full versus the rate when the cavities are empty.

2.5.2 The Tracker

The ND280 tracker, installed downstream the P0D, consists of three time projection chambers (TPC) and two fined grained detectors (FGD). This set of sub-detector is optimized to study charged current (CC) interactions, in particular the charged current quasi-elastic (CCQE) process $\nu_{mu} + n \rightarrow \mu^- + p$. The tracker's main objectives are to measure the ν_μ and ν_e fluxes and spectra, in addition to neutrino interaction cross-sections.

TPC: Time Projection Chamber

The TPCs, of which there are three, perform three key functions in the near detector. First, with their excellent imaging capabilities in three dimensions, the number and orientations of charged particles traversing the detectors are easily determined and form the basis for selecting high purity samples of different types of neutrino interactions. Secondly, since they operate in a magnetic field, they are used to measure the momenta of charged particles produced by neutrino interactions elsewhere in the detector, and therefore determine the event rate as a function of neutrino energy for the neutrino beam, prior to oscillation. Finally, the amount of ionization left by each particle, when combined with the measured momentum, is a powerful tool for distinguishing different types of charged particles, and in particular allows the relative abundance of electron neutrinos in the beam to be determined.

FGD: The Fine Grained Detectors

The FGDs, of which there are two, provide the target mass for neutrino interactions that will be measured by the TPCs. The FGD will also measure the direction and ranges of recoil protons produced by CC interactions. This will give clear identification of whether an event is CCQE or not. The FGD modules consist of layers of finely segmented scintillating tracker bars. The first FGD module will consist entirely of plastic scintillator. The second will consist of part plastic scintillator and part water. In the second FDG, water is present to allow the separate determination of exclusive neutrino cross-sections on carbon and on water for comparative measurements with respect to those taken by Super-K.

2.5.3 ECAL: The Electromagnetic Calorimeter

The ND280 electromagnetic calorimeter (ECAL) surrounds the P0D and the tracker. It consists of plastic scintillator bars, read by a wavelength shifting (WLS) fiber connected to a mulit-pixel photon counter (MPPC) [see Ch. 3 for further details on the MPPC], interleaved with lead absorber sheets. Its coverage is almost hermetic in that it will detect any charged particle leaving or entering the inner volume of the ND280. The ECAL's main goal is to measure the energy and direction of the outward (or inward) going charged particles through the detection of photons. The ECAL also plays a key role in the measurement of π^0 production. The ECAL is made of 13 independent modules: six modules surround the tracker volume on the four sides parallel to the beam axis (Barrel ECAL), one module is placed downstream the tracker (Ds-ECAL), and six modules surround all six sides of the P0D [see Fig. 2.9a].

Chapter 3

The Side Muon Range Detector

This chapter describes physical layout of the Side Muon Range Detector, or SMRD for short. Herein, a top down description will be given, where we will first describe the functional role of the SMRD. Next the UA1 magnet that houses the SMRD will be discussed, and then we will describe the scintillator modules of the SMRD, and finally discuss the individual components which the modules are constructed from. As the SMRD is housed inside the magnetic yoke this provides part of the physical design constraints, and this is on top of any financial constraints.

3.1 The Role of the SMRD

The SMRD serves three primary functions as part of the ND280 off-axis near detector: (1) the SMRD measures muons produced in neutrino interactions that cannot be well reconstructed by the detectors located in the tracker section, (2) the SMRD detects cosmic ray muons for the purpose of calibration triggering, and (3) it vetoes muons that come from sources outside of the ND280.

3.1.1 Muon Measurements

The most important tracks to be measured by ND280 detectors are those of muons, since the neutrino energy reconstruction relies primarily on muon reconstruction. In fact, the reconstruction for the most abundant CCQE events are based only on the reconstruction of the momentum of outgoing muons. The TPC gas chambers in the tracker are the best for this purpose, since they offer good tracking capabilities and momentum reconstruction via measurement of track curvature. It has been estimated that the track in the TPC must be at least 60cm long in order to effectively reconstruct a muons momentum. This suggests that there is a class of tracks that needs to be handled by other sub-detectors - a role fulfilled by the SMRD. These particular tracks are primarily those that whose trajectory are nearly perpendicular to the beam axis, i.e. they traverse the FGD they were created in, cross one of the ECals and enter the SMRD.

The SMRD can roughly measure momentum (using range information) and direction of a muon track,

where direction estimation requires at least two hits left by the muon. While the precision of SMRD measurements are less than the precision of TPC measurements, they still provide useful information. SMRD measurements can also supplement those taken by the TPCs.

3.1.2 Calibration Function

The ND280 detector makes use of cosmic ray muons as one of the methods of calibration. This method utilizes the fact that neutrino interactions in the detector occur only when beam spills arrive - no neutrino measurements are conducted between the consecutive spills. This allows us to perform other measurements in between spills or while the beam is not active.

The calibration measurements described here use cosmic ray muons as the calibration signal. The muons, produced in the atmosphere as a result of cosmic ray interactions, cross the detector producing a signal in the SMRD at an average rate of 4600 counts per second. Sub-detectors can verify operation by looking at the signals produced by these traversing muons.

The SMRD plays a role of a trigger in this procedure. A signal detected in scintillators in six different sides of the ND280, of which the SMRD serves as top, bottom, left and right, indicates a passing muon. The response of the sub-detectors in the basket can be compared for verification and compared to see if they coincide. If they deviate from the expected response, then appropriate system check and calibrations can be made. In like manner, detector efficiencies can be determined via this method. The calibration is done once before the start of the experiment. Then, throughout its operation, the same procedure is used to monitor the ND280 and to recalibrate or signal maintenance of appropriate sub-detectors as needed.

3.1.3 Veto Function

When the beam spill arrives it is important to be able to measure neutrino interactions from inside the detector only while discarding tracks that enter the detector from outside. Tracks that would originate in outside the ND280 derive from cosmic ray muons and various interactions in the rock surrounding the pit whic houses the ND280. Since the SMRD is the outermost sub-detector of the ND280 off-axis near detector, it is the most convenient tool for ruling out tracks that originate outside the detector. The exclusion procedure can be based on the time correlation between signals the hits in SMRD will occur at earlier times than hits in the inner detectors in the basket. The SMRD's time resolution is less than 2 ns, when taking into account two signals from both ends of a single scintillator.

3.2 The Magnet Yoke

Each clam[1] of the UA1 magnet yoke is made of eight segments and each of those segments are referred to as a C because of its shape [see Fig. 3.1]. A single C consists of 16 layers of iron, expanding radially outwards. The layers are constructed from 48 mm thick iron plate, and have 17 mm air gaps between them. The spacers are separated evenly, splitting the gap into 12 azimuthal sections. Four of these sections

[1]The left half of the magnetic yoke is referred to as the left-clam; whereas the right half is referred to as the right-clam

(a) (b)

Figure 3.1: 3.1a shows a schematic diagram of a single C of the magnet. 3.1b shows a close-up photo of the gaps in a C of the magnet.

are in the corners, meaning the size varies with the layers, but the eight remaining sections have gaps of constant size, $876 \times 910 \times 17$ mm^3 for the horizontal (top and bottom) and $876 \times 700 \times 17$ mm^3 for the vertical (left and right).

Hence, each C of the magnetic yoke has 8 sections known as towers - 2 on the top, 2 on the bottom, and 4 on the side. As each C is constructed from 16 layers of iron, then each of these 8 towers has 15 gaps, and each clam has 8 C's. Hence, each C could hold 120 scintillator modules and the entire magnetic yoke has the capacity for 1920 scintillator modules.However, due in part to budget constraints, only a selection of the gaps are filled with plastic scintillator modules.

The selection of which gaps to fill with scintillator modules is based on two of the functions of the SMRD. First, it is desirable to maintain good reconstruction of muons produced in neutrino interactions inside the tracker, particularly those that cannot be reconstructed elsewhere. Second, it is desirable to maintain the capability of the SMRD to efficiently trigger calibration events, i.e. ability to see cosmic ray muons in the yoke.

In order to accomplish the first goal, Monte Carlo studies were done which revealed several asymmetries in the trajectories of muons produced in neutrino interactions inside the tracker.

1. Forward/backward asymmetry: more muons are collected in the downstream parts of the detector.
2. Lateral/horizontal asymmetry : more muons reach lateral parts of the magnet yoke.
3. Up/down asymmetry: bottom parts are more populated than upper ones.

Additionally a 2 out of 3 type logic was developed where:

- To give a sub-trigger (a trigger in one part of the yoke), a muon has to light up at least two of three (or more) scintillator layers in a single tower located in that part.

- Two sub-triggers in different parts of the yoke add up to a calibration trigger.

For this method to work we have to have at least three layers of scintillators at hand in each side of the yoke.

Taking the above into account, the final SMRD layout was decided upon. All towers with horizontal gaps, i.e. the top and bottom towers, have 3 layers of modules each and since there are 64 such towers, 32 on top and 32 on the bottom, then there are a total of 192 horizontal scintillator modules. In the towers with vertical gaps, yokes 1 - 5 have 3 layers of modules, yoke 6 has 4 layers of modules, and yokes 7 - 8 have 6 layers yielding a total of 248 vertical scintillator modules.

3.3 SMRD Scintillator Modules and Counters

The dimensions of the detector modules are constrained by the dimensions of the gaps in the yokes. Horizontal modules [see Fig. 3.2b] measure 9 mm $\times$ 686 mm $\times$ 955 mm, while vertical modules measure 9 mm $\times$ 892 mm $\times$ 955 mm. Due to the differently sized spaces for horizontal and vertical gaps, horizontal SMRD modules consist of 4 scintillation counters and vertical SMRD modules consist of 5 scintillation counters. Hence, the SMRD consists of 768 horizontal and 1240 vertical scintillation counters - 2008 counters in total.

Extruded Aluminum H-profiles are used to inter-connect counters into modules and edges of the first and last counter in each module were protected with aluminum U-channels. Counters and the extrusions are tightly wrapped with capton tape in three locations. Additionally, to stabilize the modules inside a magnet slit tape springs made of phosphorbronze are mounted on both sides of the modules.

Just as the horizontal and vertical modules differ in dimensionality, likewise the horizontal and vertical counters are of different dimensions in order to maximize the used space inside the gaps of the magnetic yoke. The individual horizontal counters have dimensions of 7 mm $\times$ 167 mm $\times$ 875 mm; whereas vertical counters measure 7 mm $\times$ 175 mm $\times$ 875 mm. Each counter is constructed from polystyrene which does not naturally scintillate, so two different dopants are added during extrusions - 1.5% PTP and 0.01% POPOP.

Embedded in a 1.1 mm milled groove in the polystyrene scintillator slab is an serpentine shaped 1 mm diameter Y11 (150) Kuraray WLS fibers of flexible 259 S-type and with double-cladding. the purpose of the serpentine-shaped fiber si that it results in near uniform response across the surface of the scintillation counter and minimize the number of photosensors, in this case MPPCs, and electronics channels compared to more conventional multiple straight fiber type design.On each end of the counter is an endcap that features a snap-on mechanism to engage a connector with an inserted Hamamatsu multi pixel photon counter (MPPC), to couple to the endcap and theWLS fiber ferrule, respectively. The MPPCs are backed by a foam-spring to ensure a reliable connection between the photosensor front face and the polished WLS fiber ends [see Fig. 3.2a].

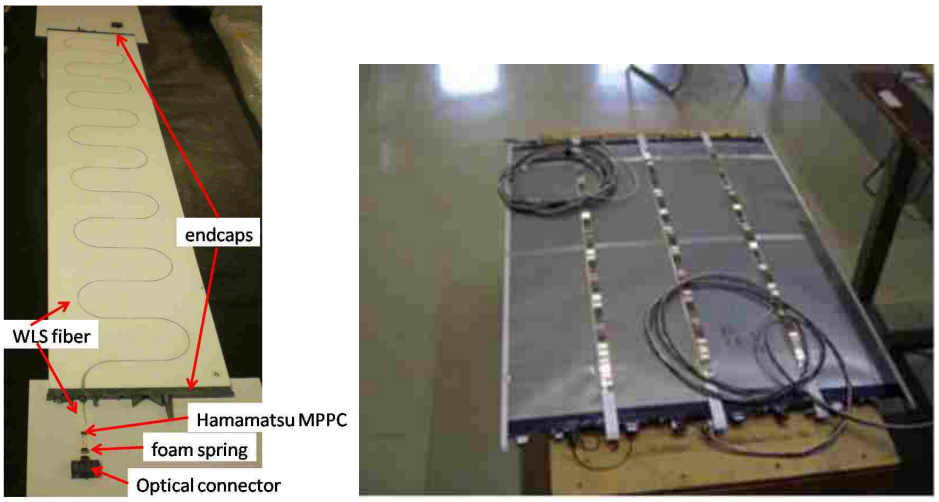

(a) (b)

Figure 3.2: The photo in 3.2a shows a single scintillator counter with its various parts labeled. 3.2b shows a completely assembled horizontal SMRD module.

3.4 The Multi-Pixel Photon Counter

Figure 3.3: The full view of the MPPC is shown in th above photgraph.

All light signals from the counters in the SMRD are transported by the WLS fiber and transformed into electric signals by MPPC photodiode sensors. A Multi-Pixel Photon Counter [see Fig. 3.3] is an array of photodiode pixels. Each pixel operates above its breakdown voltage (approximately 70V) and can produce an avalanche of electrons when struck by a photon. The MPPCs selected for use throughout the ND280 are the Hamamatsu S10362-13-050C which provides the single photon counting capability and the electronic gain of a traditional photomultiplier, but is less expensive and can operate in an environment where magnetic field is present as it is impervious to such. The active area of the device is a square area 1.69 mm^2, which is separated into 667 distinct 50 $\times$ 50 μm^2 pixels, where a 3 $\times$ 3 pixel block is removed from one corner for connections [see Fig. 3.4]. Each pixel is an avalanche photo-diode (APD) running in Geiger mode, where a reverse bias voltage V_{OP} greater than the breakdown voltage V_{BD} has been applied.

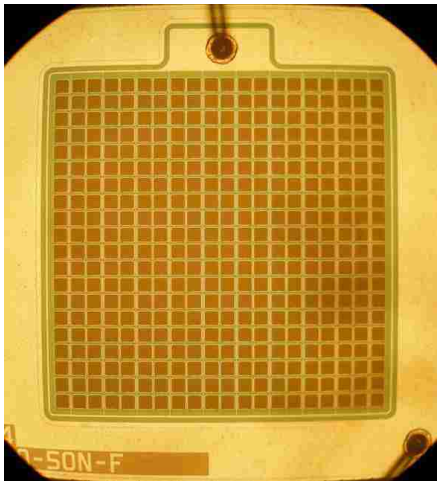

Figure 3.4: A zoomed in view of the MPPC's pixel array only is shown above.

Figure 3.5: The above photo shows a Trip-t Frontend Board used for MPPC signal read out.

Overall, the ND280 off-axis detector uses a total of ∼50.000 MPPCs. The SMRD Itself has 4016 MPPCs.

These sensors are read out to Trip-t Frontend Boards [see Fig 3.5]. The Trip-t chip, which was developed at Fermilab for the D0 experiment, provides time and charge for any discriminated pulses, with nominal time resolution of 2.5 ns. The boards also provide the high voltage current required for proper MPPC functioning.

Chapter 4

Data Quality Considerations for the SMRD

As with all measurement devices, the SMRD can experience errors or failures. In order to ensure that data taken with the SMRD is data usable for analysis, weekly checks are performed by reviewing parameters that may indicate a malfunction with the detector itself. Data that has been taken while the detector is operating at less then optimal performance can result in faulty physics analysis as it my provide erroneous results. Depending on the severity of the problem an entire time period may be flagged as unusable or the data my still be salvaged by making adjustments in appropriate databases. Hence, the purpose of the following data quality checks is to verify the optimal performance of the SMRD and in so doing prevent erroneous physics analyses.

Three data runs, as outlined in Table 4.1, have been taken through 4/25/2012, and while Run III continues at the time of writing we have provide the most recent available data. The data quality analysis presented herein, while not entirely new, is new in that Run III is the first run to not only have these specific parameters checked, but also the first Run to have these checks produced automatically. Similar data quality analyses were produced for Run I and Run II they were processed manually which was time consuming. Although Run III has the checks processed automatically, saving considerable time, their validation is still checked manually by the SMRD Data Quality Expert, and the results are presented at the T2K Data Quality meeting where other Data Quality experts may voice concerns and give improvement suggestions.

Table 4.1: The above table shows the various runs, the corresponding start and end dates, and the number of protons on target (POT) for that particular run.

Run	**Start Date**	**End Date**	**POT**
I	1/23/2010	6/25/210	3.26×10^{19}
II	11/18/2010	3/10/2011	3.75×10^{19}
III	12/26/2011	4/25//2012	6.06×10^{19}

4.1 The SMRD Data Quality Report: Construction and Contents

Each week a report will be compiled containing data quality information for the Side Muon Range Detector (SMRD). The report will focus on the previous week of beam data, where the previous week is defined as running from the previous Sunday at midnight to the most recent Sunday at midnight. The automated data processing system was tested on the last week of data collected during Run II. Unless otherwise noted all plots herein are taken from that week, the calendar week running from Sunday 3/6/2011 to Saturday 3/12/2011.

As each calibrated `.root` file is written to disk on the semi-offline cluster the C++ program `smrd_er_n_timing.cxx` runs using this calibrated `.root` file as input and produces as output a flat tree named `ER`. Each entry in the tree corresponds to one SMRD Recon Hit, where an SMRD Recon Hit is defined as the triggering of both of the Multi-Pixel Photon Counters (MPPC) on a single counter having a 23 ns time coincidence.

4.2 SMRD Data Quality Plots

4.2.1 Hits and Timing Plots

Once per week the following SMRD data quality plots are produced:

- Reconstructed Hits per 12 Hour Period
- Mean Timing Values for the 8 Bunches
- Timing Width of Each of the 8 Bunches
- Time Interval Between Each of the 8 Bunches

In order to produce these plots smaller pieces of data recorded during the week ar combined into one large piece of data representing the entire weeks recorded data. The relevant data is then extracted from the overall weekly data set, relevant plots are created, and finally saved. Both the plots and the relevant saved data used to create the plots are accessible by the SMRD Data Quality expert from a remote server.

For these plots, each week runs as before (Sunday at midnight to Sunday at midnight) with each day divided into two 12 hour periods, where the first 12 hour period runs from midnight to noon and the second period runs from noon to midnight (all times are JST). There are therefore 14 periods for each week, and hence, 14 data points on each of the above listed plots.

Hits per 12 Hour Period

For each of the fourteen 12 hour periods the total number of reconstructed hits (as defined above),also refered to as recon hits, are computed and subsequently plotted. The number of hits in a particular period are not normalized. Although, the original intention was to plot the hits per 12 hour period normalized to protons on target (POT) as recorded at CT5, this was found to be impractical as POT data is not concurrently available on the semi-offline cluster when these plots are made.

It can therefore be difficult to make an accurate comparison in this plot from one period to the next. Expected variations in the number of POT for that period can cause appearance of a lower number of hits although there is no malfunction in SMRD operation. Case in point, the the 3rd, 4th, and 11th data points in Fig. 4.1 are low when compared to the other 8 data points which fall in the range of 70,000 to 80,000 hits (the last 3 data points are from the period just after the 2011 Tōhoku Earthquake).

Conveniently an electronic log book is kept by those working on site in Tokai, where the ND280 detector is physically located. These log entries are viewable by all collaborators on the T2K project including the SMRD Data quality Expert. In reviewing these log entries one can see what normal operations have occurred as well as any known malfunctions that have occurred. The log entries corresponding to the 3rd, 4th, and 11th data points in Fig. 4.1 indicate that the neutrino beam was shut down during each of these time periods. When the neutrino beam is shut off then less activity, i.e. less hits, is expected in the SMRD.

Since all periods demonstrating a lower number of hits are related to the absence of beam activity and not to the malfunction of the SMRD, related electronics malfunctions, or Data Acquisition (DAQ) problems, then this plot would give no indication of data quality concerns.

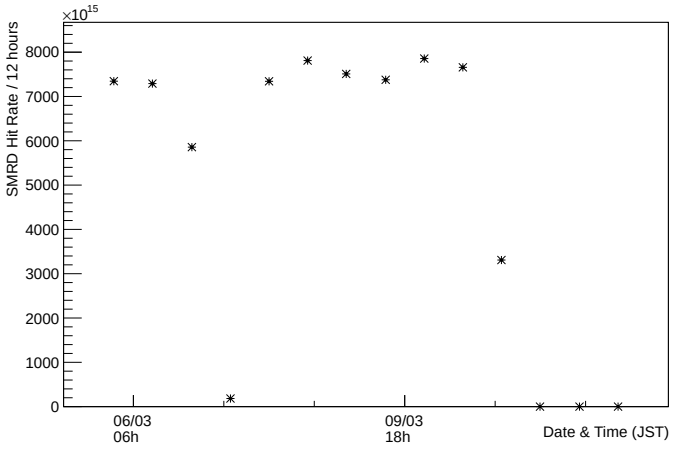

Figure 4.1: Total number of Recon hits [those with a 23 ns time coincidence] in each of the fourteen 12 hour periods during the week of 03/06/2011.

Mean Timing Values for the 8 Bunches

During Run 2 the beam has an 8 bunch structure and this is expected to continue through Run 3. For each of the 14 weekly 12 hour periods there are 23 timing buckets into which each recon hit falls. Two separate plots are made. The first of these two plots has 8 timing buckets which correspond to the 8 bunches of a

neutrino beam spill [see Fig. 4.2]; whereas the second plot has 15 timing buckets (4 before the 8 buckets corresponding to the beam bunches and 11 after) [see Fig. 4.3]. Each of the 8 bunches corresponding to the beam spill are Gaussian fit to find the mean time of detection in the SMRD [see Fig. 4.2]. The eight bunch Gaussian fit is done for each twelve hour period throughout the week and each fit itself is stored in the iRods data system along with the other relevant SMRD data. The overall plot showing the mean bunch timing for each of the 12 hour periods is shown in Fig. 4.4.

In Fig. 4.4 the mean times for each of the bunches is plotted along with error bars, although they are not visible due to the large scale of the graph. The timing of the bunches appears stable when the graph is viewed at this scale. In Fig. 4.5, however, the graph scale has been expanded to show only the second bunch and the variance in timing can be seen for this particular bunch during the week plotted, not to mention the visibility of the graphed error bars. In particular the error bars for the 4th data point representing the noon to midnight period on March 7, 2011 are visible and as previously mentioned this resulted from low statistics due to a beam shut down.

As seen in Fig. 4.5 Bunch timings may vary during the week. However, some variation is to be expected. It becomes a concern when the variation in bunch mean timing is larger than the expected 1σ bunch width of 20 - 30 ns. As seen in Fig. 4.5 the variation is smaller than the expected 1σ bunch width and hence, this variation in meant timing is not a concern.

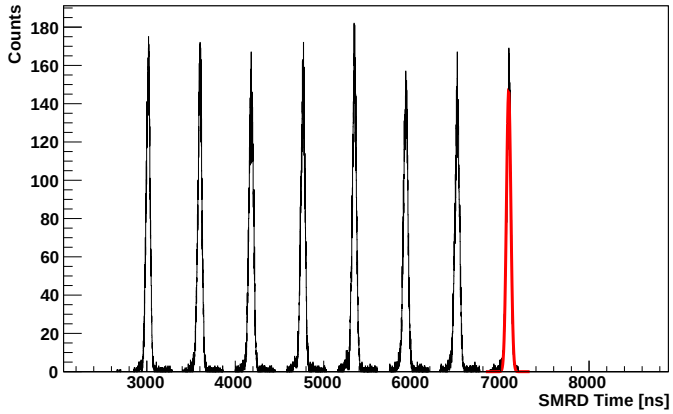

Figure 4.2: Plot of the 8 bunch structure evident in the timing window corresponding to the beam spill. Also shown, as an overlaying red line, is the Gaussian fit for the eighth bunch.

Timing Width of Each of the 8 Bunches

When the Gaussian fit for each of the eight bunches is done, not only are the mean values plotted for each of the eight bunches, but the bunch widths are also plotted as shown in Fig. 4.6. In the graph shown in Fig. 4.6 each of the 12 hour periods for the week has 8 data points, one data point for each of the eight bunches.

It is readily evident the there is a problem with the bunch width for the 4th 12 hour period. This is demonstrated by the wide range the width values for this period as well as the large range of the error bars for each data point in this period. This stems from the low statistics for the period causing the Gaussian fits for this period to have lower peaks and wider widths. The low statistics of this period are due to the

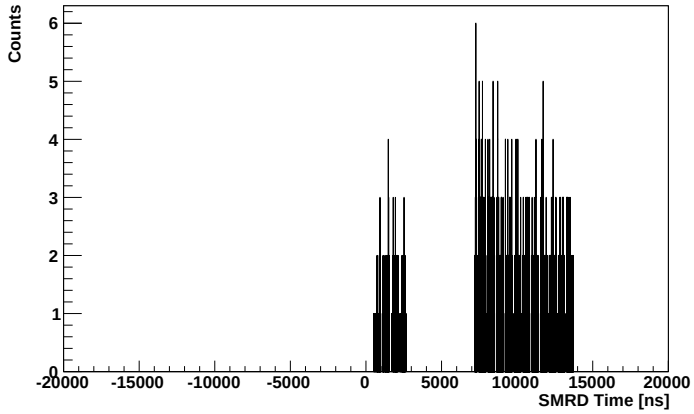

Figure 4.3: Plot of the 15 timing buckets occurring outside of the timing window corresponding to the beam spill. The gap in between the 4 timing buckets on the left and the 11 timing buckets on the right is where the 8 timing buckets [see Fig 4.2] corresponding to the beam bunches would fit.

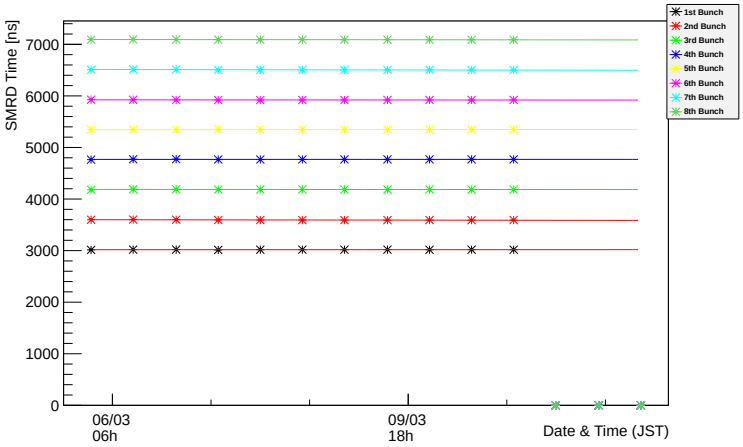

Figure 4.4: Graph showing the mean timing values of each of the 8 bunches for each of the fourteen 12 hour periods during the week of 03/06/2011. A linear best fit line is shown for each of the 8 bunches. Error bars are plotted for each data point but are not visible at this scale.

low activity which is caused by the amount of time the beam is off for this 12 hour period. While the width of these bunches does not fit in the expected range, this in no way constitutes a malfunction of the SMRD.

As a whole the T2K Data Quality Group has chosen this data set, not because it demonstrates what an ideal week would look like, but because it is an actual week of full data taking with minimal down time. In using the actual data taken during the week of 3/6/2012 we want to see what types of problems could be encountered during a normal week of activity, since Run III is to be the first run of data taking with this particular setup of SMRD data quality checks. By encountering non-ideal circumstances we have a chance to develop methods of system checks and verifications that smooth out the process when running. These plots for the week of 3/6/2012 were created during the Fall of 2011 prior to the beginning of Run III. The SMRD data quality setup created during these automation tests in the Fall of 2011 have been implemented during Run III and continue to be developed in an ongoing manner.

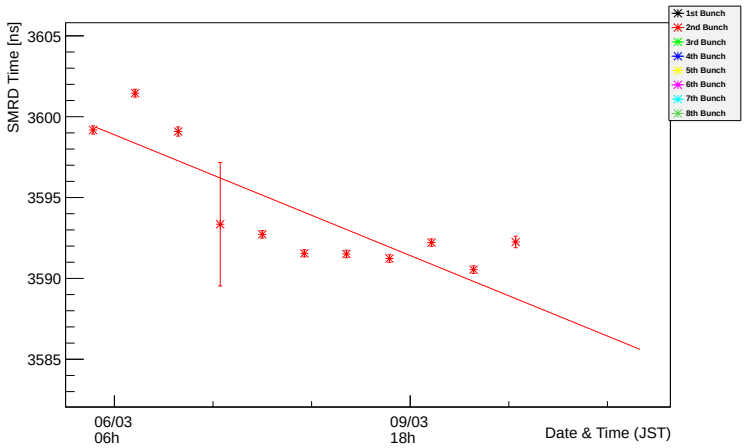

Figure 4.5: Graph showing the mean timing values of the 2nd bunch for each of the fourteen 12 hour periods. The linear best fit line for the 2nd bunch shows that the mean timing value has decreased during the week of 03/06/2011.

However, the other 12 hour periods have their data points confined to a much narrower range between approximately 22 and 25 ns [see Fig 4.7]. We normally expect the bunch widths to be 23 ns with slight variations and therefore the bunch widths other than the 4th 12 hour period appear to be within an acceptable range.

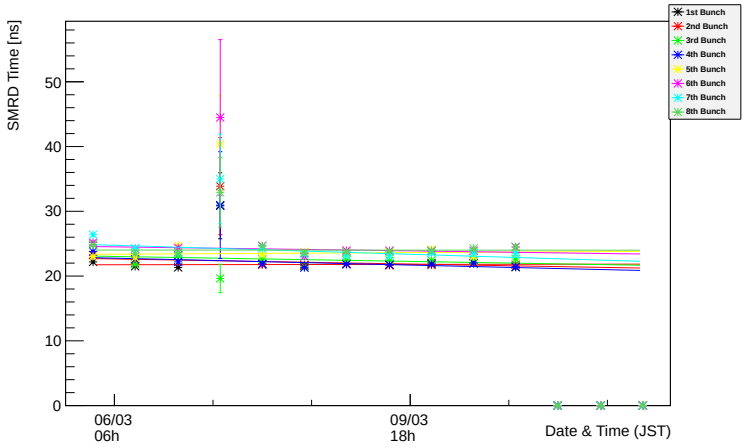

Figure 4.6: Graph showing the bunch widths of each of the 8 bunches for each of the fourteen 12 hour periods during the week of 03/06/2011. Error bars are plotted and are evident for the 4th 12 hour period.

Time Interval Between Each of the 8 Bunches

The time interval between two bunches is calculated by taking a mean timing value for a specific period and subtracting from it the mean timing value for the previous period giving seven intervals to be calculated. For example, the first interval is calculated by subtracting the mean of the first period from the mean of the second period to yield the "2nd - 1st bunch" interval.

Figure 4.8 shows the seven intervals for each of the fourteen 12 hour periods. Since the last three periods

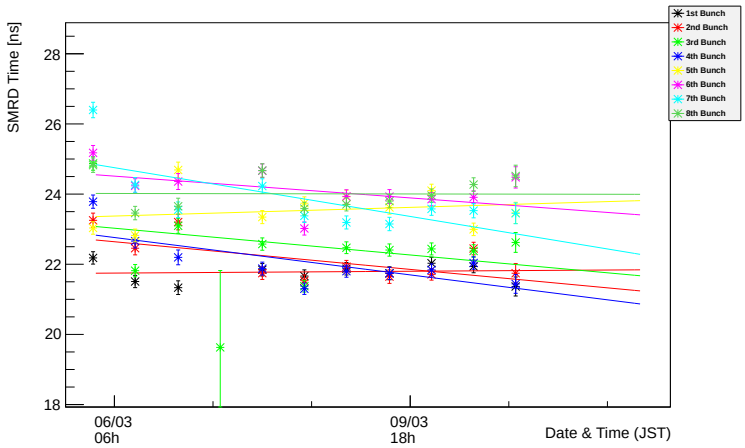

Figure 4.7: An expanded scale of the plot showing the timing widths of each of the eight bunches. Most values are near the expected value of 23 ns.

contain no data the linear fit for each interval is skewed. However, when the scale on the y-axis, representing the interval time in ns, is expanded it is clear that the calculated values for the time intervals are centered about 581 ns [see Fig. 4.9]. The fact that the time intervals are centered around 581 ns is exactly what we expect; and when this is coupled with the fact that the last three 12 hor periods are expected to have no data we can conclude that the interval between the bunches indicates no problem in relation to data quality.

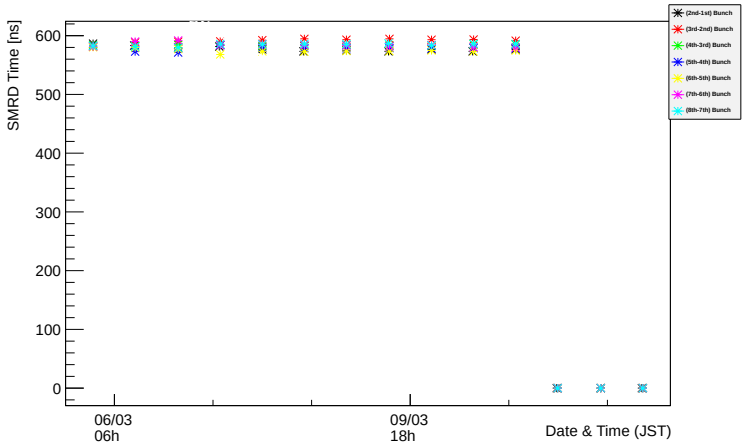

Figure 4.8: Graph showing the time interval between each of the 8 bunches for each of the fourteen 12 hour periods during the week of 03/06/2011.

4.2.2 SMRD Gain and Pedestal Plots

Each week pedestal and gain values are plotted for the overall SMRD as well as for each of the RMM's. Each of the following plots has the same general 2D histogram format. The x-axis is the time axis showing when the plotted value was sampled, whereas the y-axis is the number of ADC counts. The color scale on the 2D histogram represents the number of channels at that given ADC count (y value) at the time period

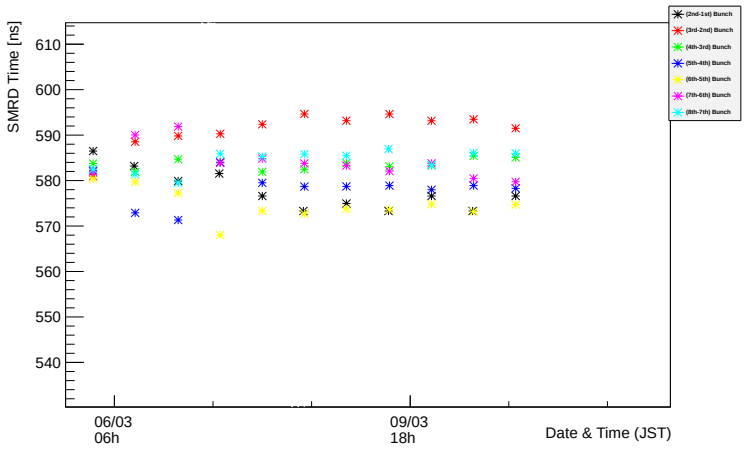

Figure 4.9: An expanded scale of the plot showing the timing intervals of each of the eight bunches. Values are centered around the expected value of 581 ns.

when sampled (x value). Values are sampled approximately every 3 hours.

In addition to the actual gain and pedestal values, drift values are plotted for pedestal values as well as gain values. The drift values are plotted using the same 2D histogram format described above.

Lastly, we plot dead channels and bad channels using a graphical format showing the total number of channels (y value) that are either dead or bad at a given time (x value). The detailed channel info and associated error info is also recorded in two text files called `gain.log` and `ped.log` both of which are stored in iRods.

High and Low Gain Pedestal Plots

Pedestal values are plotted for both the high gain channels and for the low gain channels. These are subdivided by RMM, and thus there is one plot per RMM for both the high gain channels and the low gain channels yielding a total of eight plots. The plots for the high gain channels are shown in Fig. 4.10 whereas the plots for the low gain channel are shown in Fig. 4.11.

It is clearly visible that the plots shown in both Fig. 4.10 and Fig. 4.11 have scale on the y-axis that is larger than the range that contains the greatest density of values. The purpose of this large y range is to allow us to catch pedestal values outside the expected range such as those shown early in the week (left side of the plot) on Fig. 4.10a. These larger than expected high gain channel pedestal values do not continue to appear throughout the week indicating they have returned to the expected range. These out of range channels can be crosschecked via the text file `ped.log`.

High and Low Gain Pedestal Drift Values

The High/Low channel pedestal value taken at the beginning of the week is used as reference value to calculate a drift value for that specific channel, where the drift values is defined to be the difference between the reference value and the current value. Therefore, all channels should have a drift value of

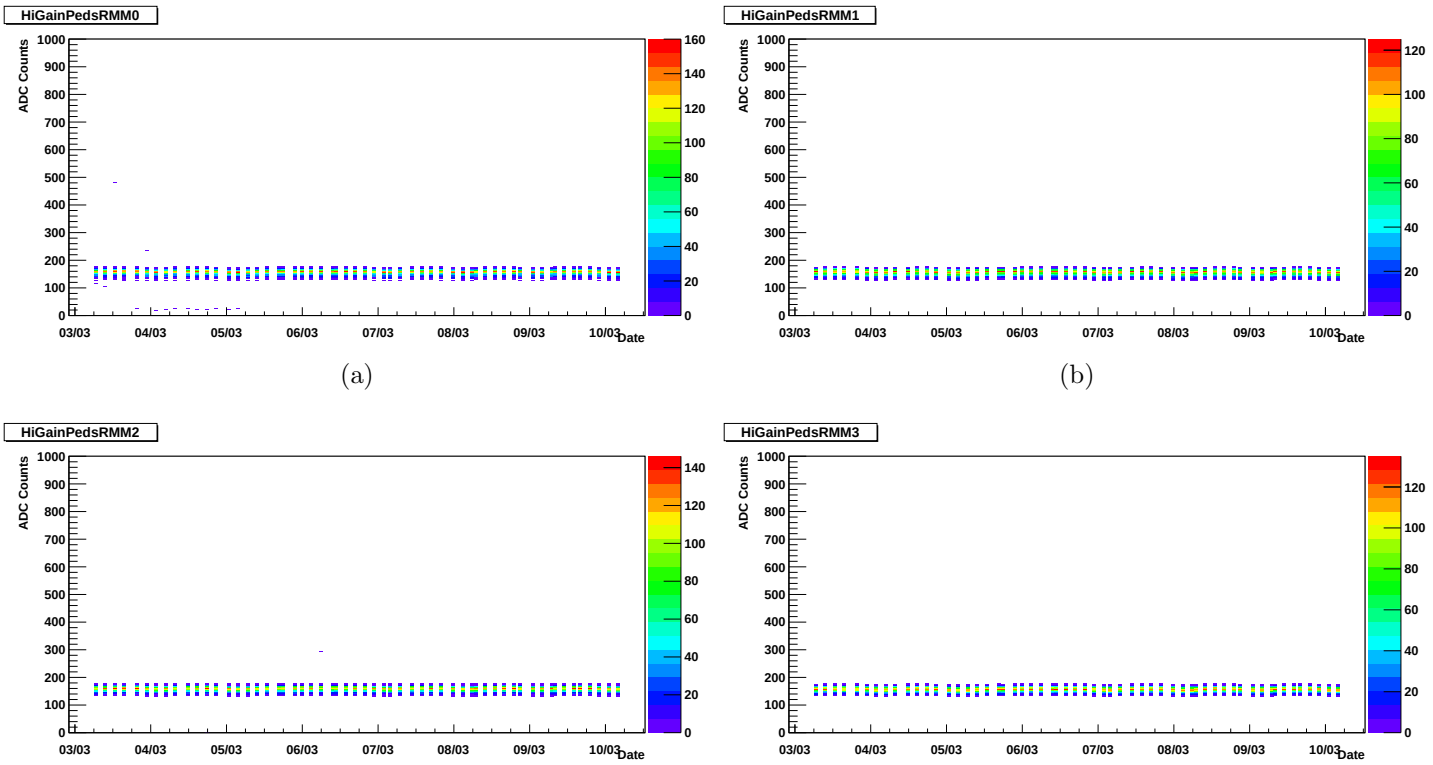

(a) (b) (c) (d)

Figure 4.10: Shown above are the pedestal plots for the high gain channels divided by RMM. 4.10a displays the values for RMM0, 4.10b displays the values for RMM1, 4.10c displays the values for RMM2, and 4.10d displays the values for RMM3. The color axis represents the number of channels at that ADC count value.

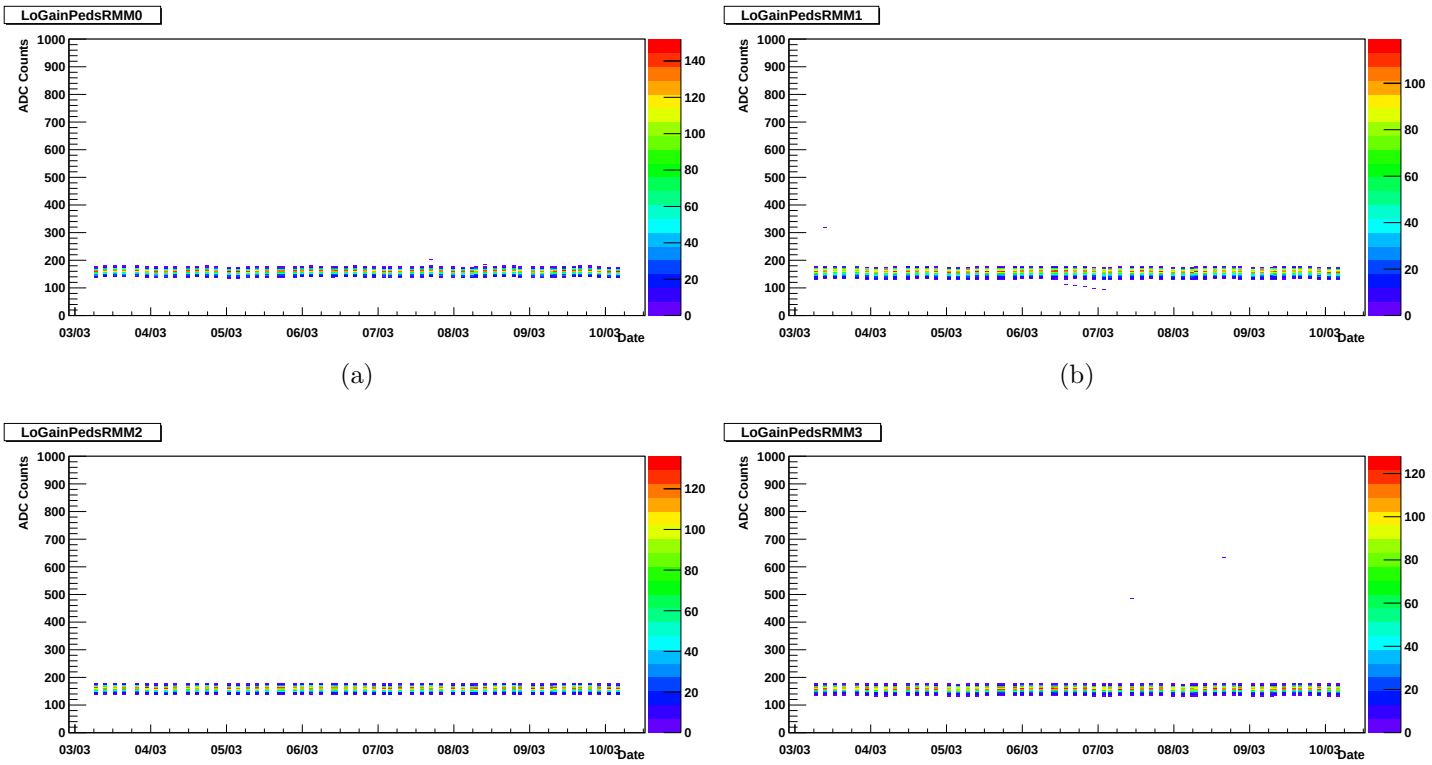

(a) (b) (c) (d)

Figure 4.11: Shown above are the pedestal plots for the low gain channels divided by RMM. 4.11a displays the values for RMM0, 4.11b displays the values for RMM1, 4.11c displays the values for RMM2, and 4.11d displays the values for RMM3. The color axis represents the number of channels at that ADC count value.

0 ADC counts at the very beginning of the plot. For both High and Low channels a single plot for all channels is created [See Fig. 4.12 and Fig. 4.14] as well as one plot for each RMM [see Fig. 4.13 and Fig. 4.15]. In other words, there are 5 drift plots for Hi gain channels and 5 drift plots for Low gain channels - 10 plots total.

The pedestal peaks of an individual channel on the SMRD are found by fitting to find the first peak. From previous fittings the mean 1σ of the pedestal peak was found to be 1.5 ADC bins. Therefore, the range for High/Low gain Pedestal drift values was set to approximately $\pm 3\sigma$ or ± 5 ADC bins. Any drift value outside this range is sent to the `ped.log` file and recorded as a warning. Not only are these out of range values recorded in text format, but they are also plotted in graphical format [See Fig. 4.16] so that the number of channels out of range at any one time may be easily tracked.

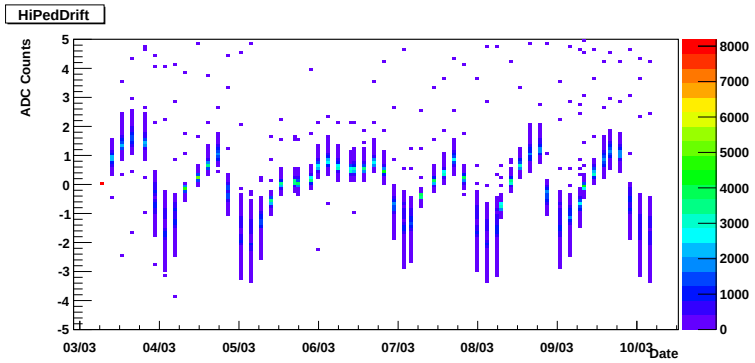

Figure 4.12: The above plot shows the drift values for all SMRD Hi Gain Pedestal Channels.

Gain Values and Associated Plots

Gain values are calculated as the difference between the pedestal peak and the first p.e. peak. Gain values are plotted for the overall SMRD as well as by RMM, so there are 5 total gain value plots, 1 per RMM and 1 overall plot [see Fig. 4.17 and 4.18]. It is expected that Gain values for MPPC / Trip-T based detectors be 10 ADC counts, which is the case with the SMRD as evidenced in Fig. 4.17 and Fig. 4.18.

Gain Drift Values

Gain drift values are calculated in a similar manner as the pedestal drift values. The gain value taken at the beginning of the week is used as reference value to calculate a drift value for that specific channel, where the drift values is defined to be the difference between the reference value and the current value. Therefore, all channels should have a drift value of 0 ADC counts at the very beginning of the plot. For gain drift values a single plot for all channels is created [See Fig. 4.19] as well as one plot for each RMM [see Fig. 4.20]. In other words, there are 5 gain drift plots - 1 overall plot and 4 corresponding to each of the RMM's.

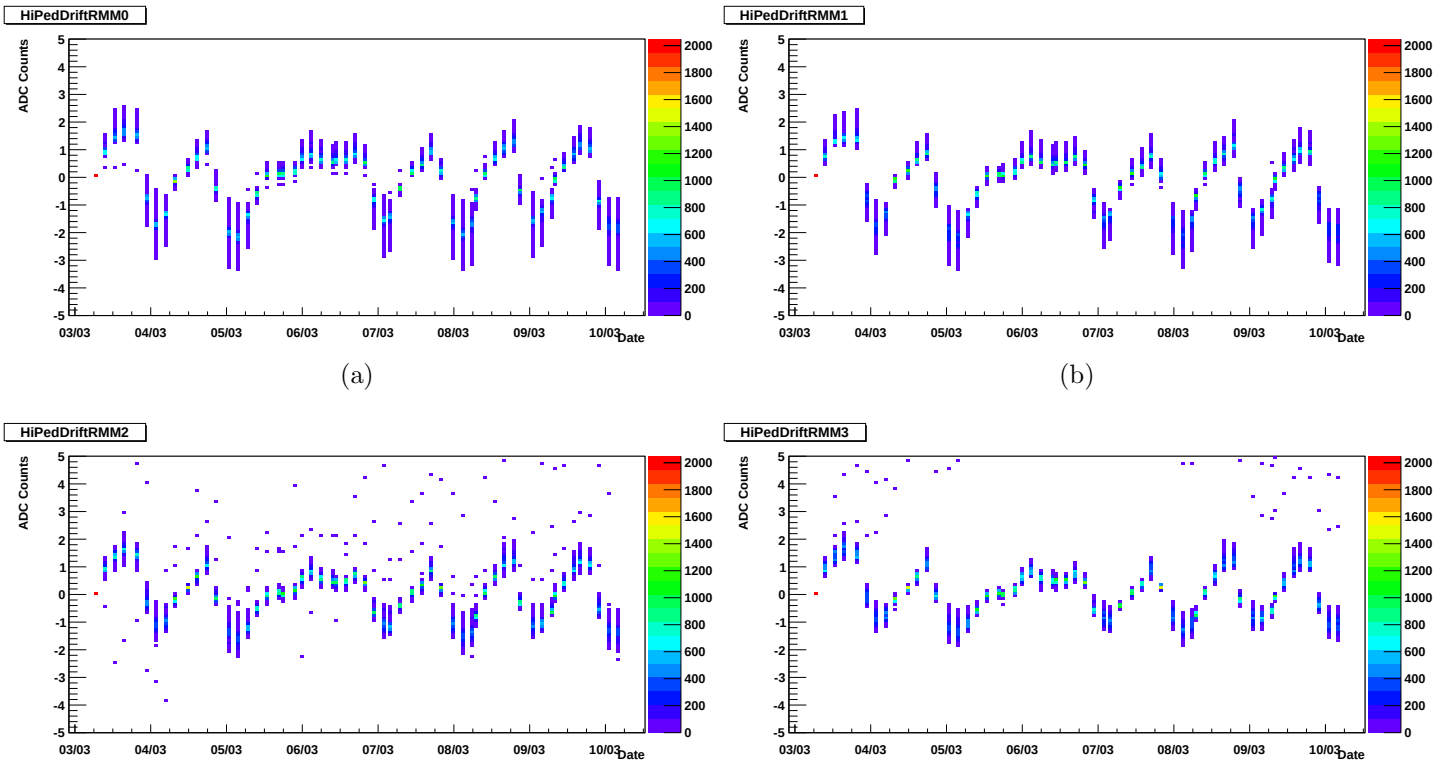

(a) (b) (c) (d)

Figure 4.13: Shown above are the drift plots for the high gain channels divided by RMM. 4.13a displays the values for RMM0, 4.13b displays the values for RMM1, 4.13c displays the values for RMM2, and 4.13d displays the values for RMM3. The color axis represents the number of channels at that ADC count value.

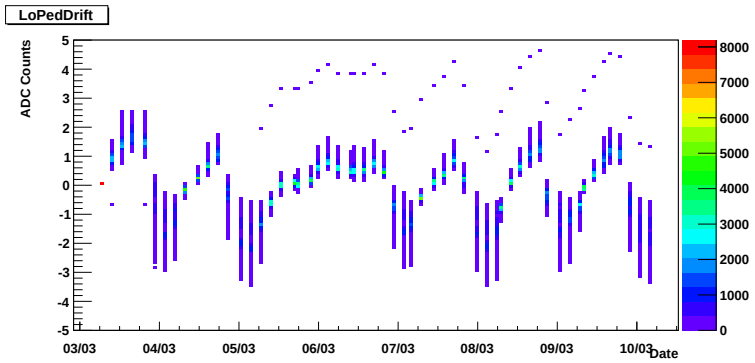

Figure 4.14: The above plot shows the drift values for all SMRD Low Gain Pedestal Channels.

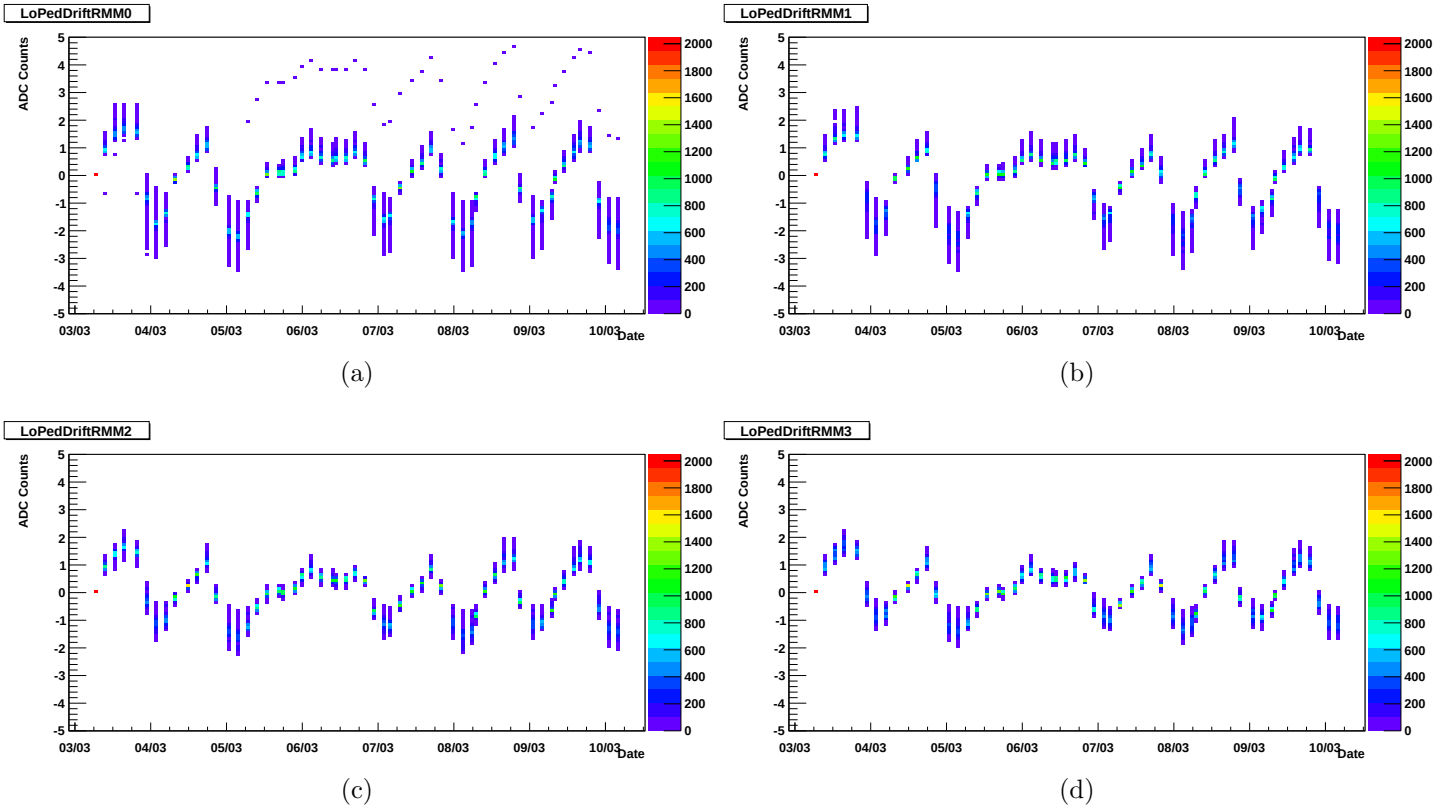

(a) (b) (c) (d)

Figure 4.15: Shown above are the drift plots for the low gain channels divided by RMM. 4.15a displays the values for RMM0, 4.15b displays the values for RMM1, 4.15c displays the values for RMM2, and 4.15d displays the values for RMM3. The color axis represents the number of channels at that ADC count value.

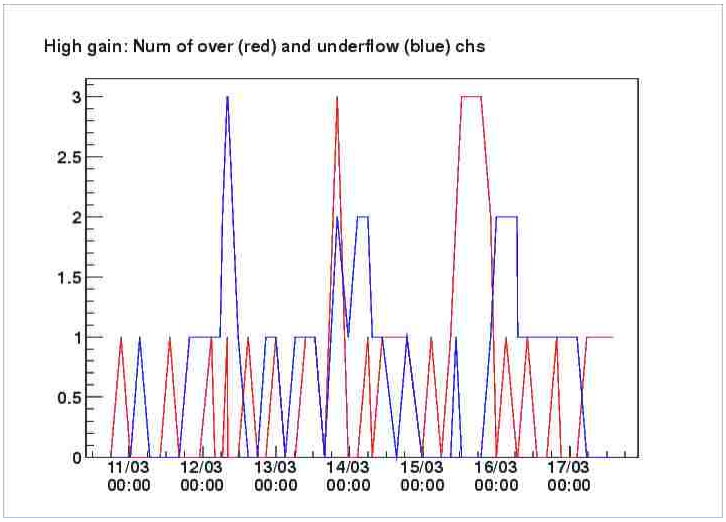

Figure 4.16: Shown above is the plot showing the number of channels outside of the ±5 ADC range for High Gain Pedestal channels for the week ending 03/17/2012. Displayed are the number of High Gain channels that have drifted over +5 ADC in red and the number of channels that have drifited under -5 ADC in blue for particular intervals during the week.

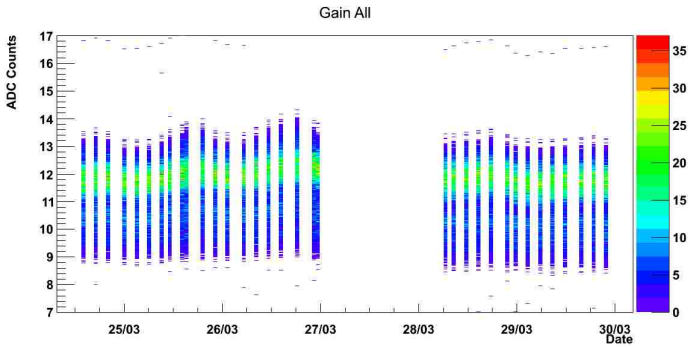

Figure 4.17: The above plot shows the gain values for the overall SMRD for the week ending 3/31/2012. The color axis represents the number of channels at that particular gain value.

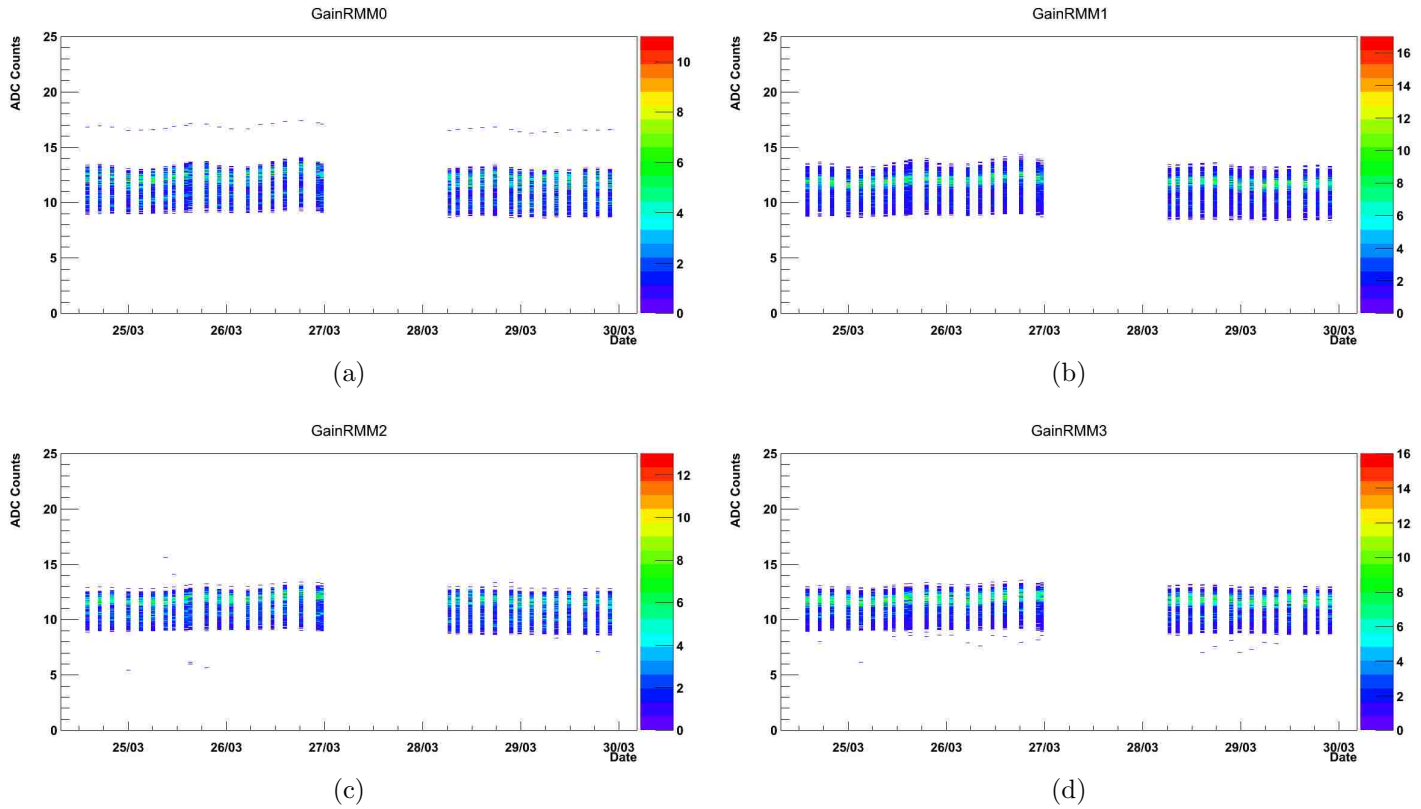

(a) (b) (c) (d)

Figure 4.18: Shown above are the gain plots divided by RMM. 4.18a displays the values for RMM0, 4.18b displays the values for RMM1, 4.18c displays the values for RMM2, and 4.18d displays the values for RMM3. The color axis represents the number of channels at that gain value.

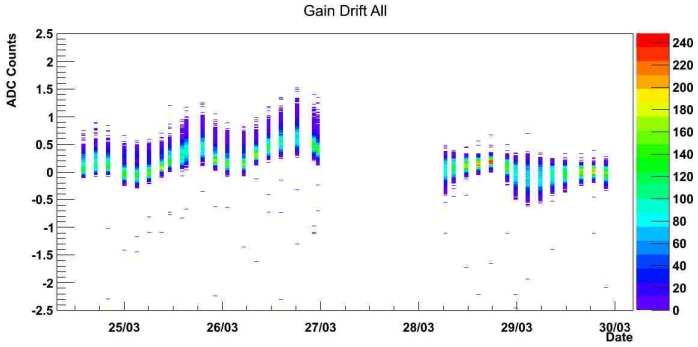

Figure 4.19: The above plot shows the gain drift values for the overall SMRD for the week ending 3/31/2012. The color axis represents the number of channels at that particular gain value.

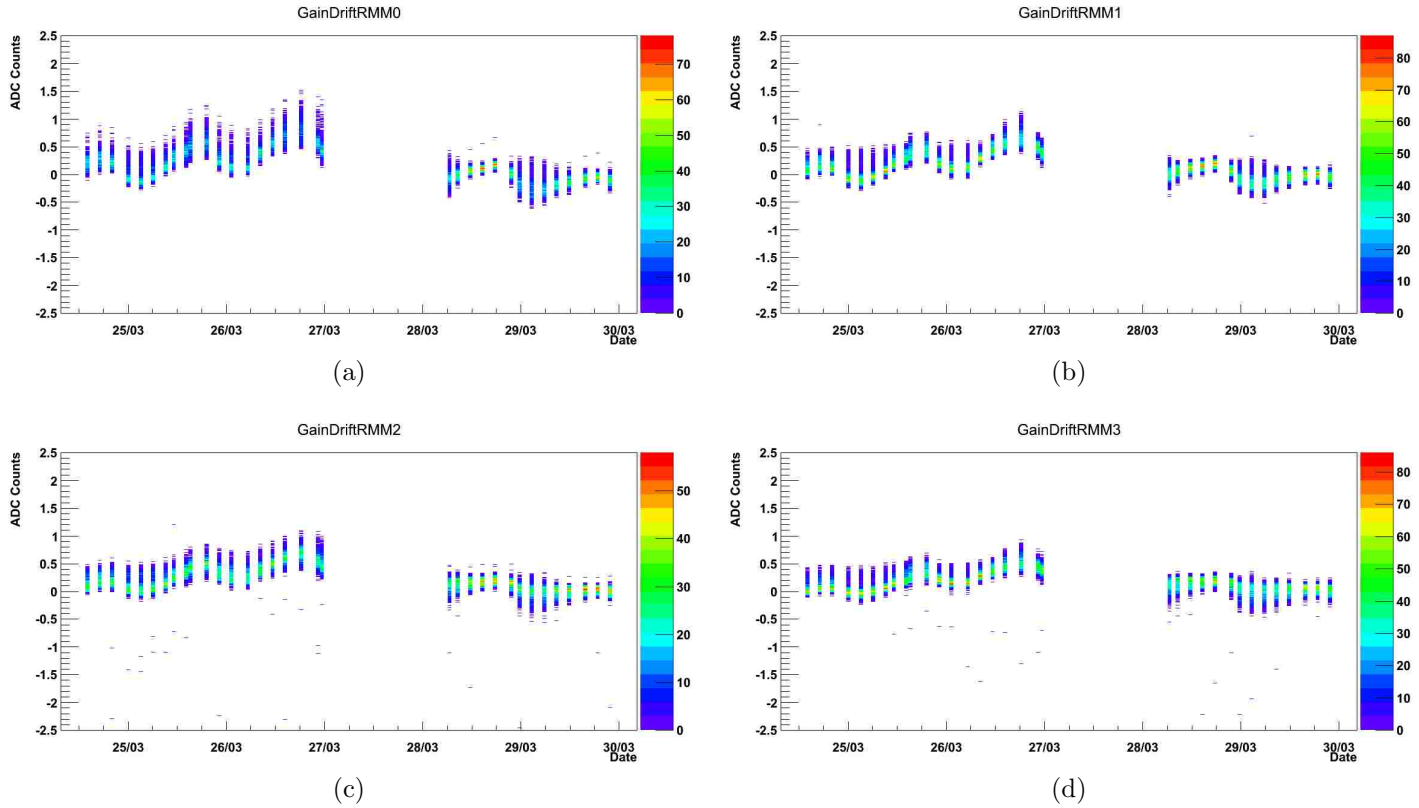

Figure 4.20: Shown above are the gain drift plots divided by RMM. 4.20a displays the values for RMM0, 4.20b displays the values for RMM1, 4.20c displays the values for RMM2, and 4.20d displays the values for RMM3. The color axis represents the number of channels at that gain drift value.

4.3 SMRD Data Quality Flag

Once the weekly parameters have been verified, the data quality flag is uploaded in to a database. The value 0 is used to signify periods of time when the detector was operating as expected; whereas any other value indicates a problem. Once the data quality flag for the SMRD is set, anyone can access the flag in the database to verify whether the data for that time period is usable or not. Problems flagged by the data quality flag may include timing synchronization problems, data acquisition problem, and others.

If we look at the data quality flag values and track them over time, we can obtain a percentage of time that the SMRD has been operating without a problem. Looking at the period from 03/18/2010 20:51:08 GMT to 4/21/2012 15:00:00 GMT there are a total of 66074932 seconds. If we eliminate time where the detector was inactive due to scheduled shutdowns we reduce the possible up time to 51339045 seconds. During that time the SMRD is flagged as "bad" for 21353 seconds for SMRD related issues. Therefore the SMRD has taken good data 99.9584% of the time it was able to over the past two years.

Table 4.2 shows the breakdown of the two types of problems the SMRD has encountered. TFB trouble covers any of various problems with a TFB that can cues problems in reading out SMRD particle detection. For example, the TFB problem may be as simple as a disconnected cable or may be a more complicated electronics problem. The MCM (Master Clock Module) missynchronization is an indication that the hit timing seen by the SMRD does not match the timing it should see. In general, the SMRD timing should be synchronized with the MCM.

As part of the data quality checks individual channel readout is also monitored - where there is one MPPC per channel. This is done when the gain values are plotted. If the gain values cannot be clearly identified from the charge spectrum channels may be labeled as "noisy". If no data is reported at all the channel may be labeled as "dead". At the time of writing there is 1 channel labeled "dead" and 12 channels labeled "noisy". Since there are a total of 4016 channels (MPPC's) then 99.676% are operating optimally.

Table 4.2: The table below shows the various problems encountered which have caused the SMRD data quality flag to be set to bad. Also shown is the percentage of the trouble they account for. as a percentage of time.

Trouble Type	**Time [s]**	**Percent of Trouble**
TFB Trouble	11002	51.524%
MCM Missynchronization	10351	48.475%
Total	21353	100%

Chapter 5

SMRD Stability

It is important to show that the SMRD operation is stable over the time period it has been operating. Detector stability carries import because it shows the uniformity of measurements taken with that detector. To say that the SMRD, or any instrument used for measurement for that matter, is stable is to say that the measurement output from the SMRD at some initial time, call it t_0, is equivalent to the measurement output at some later time t. The caveat here is that the equivalency is to within some statistical / systematic uncertainty. If the detector is stable then this allows measurements from taken at different times to be comparable. Being able to compare, or use, measurements taken at varying times is important because the T2K experiment itself will be running for several years.

Detector stability can be tested via a constant source of muons with nearly uniform rate of incidence upon the detector. Conveniently the universe provides such a source in the form of cosmic ray muons. As mentioned previously, The SMRD not only records data from the neutrino beam (referred to as a spill trigger) but also records data from comic ray muons (referred to as a cosmic trigger).

For constituting detector stability the following three metrics have been chosen:

1. Light yield of all counters for unbiased cosmic trigger plotted over time.
2. A comparison of the distribution of light yield between vertical (north and south sides) and horizontal counters for unbiased cosmic trigger[1].
3. A comparison of the distribution of light yield between vertical (north and south sides) and horizontal counters for geometrically equivalent trigger settings[2].

5.1 SMRD Cosmic Trigger Settings

The T2K ND280 Electronics system consists of detector front-end boards (TFB) and back-end boards (BEB). Several back-end bards Cosmic Trigger Module (CTM), Readout Merger Module (RMM), Master

[1]See below for detailed description
[2]See below for detailed description

Clock Module (MCM), and Slave Clock Module (SCM) share a common hardware design. The CTM provides cosmic triggers for the T2K N280 experiment two CTMs for off-axis detector and one CTM for on-axis detector and sends cosmic trigger information to the T2K ND280 DAQ system.

The T2K ND280 off-axis detector has two types of cosmic triggers - Trip-T cosmic triggers and FGD cosmic triggers. It will be the former that is of interest to us as we are concerned with the SMRD. This type of cosmic trigger will be herein referred to as a Trip-t cosmic as it is concerned with the three Trip-t based detectors - the P0D, the DsECAL, and of course the SMRD.

The SMRD is organized into 128 projective towers, with 32 towers on each of the 4 sides of the magnet yoke. Each tower is served by one TFB; hence, the whole SMRD provides 128 trigger primitives to the CTM.

The global cosmic trigger algorithm the for off-axis detector are used in this system. Its trigger primitives come from SMRD, P0D and DsECAL[3]. The P0D and DsECAL of off-axis detector do not have the projective tower structure as that of the SMRD.

The SMRD, P0D and DsECAL form a rectangular trigger box [see Fig. 5.1]. Each SMRD side of this box provides 32 trigger primitives, and both P0D and DsECAL sides provide 25 logical trigger primitives.

The 6 sides of the afore mentioned trigger rectangular box are labelled as following:

- T - top SMRD
- L - left SMRD
- B - bottom SMRD
- R - right SMRD
- P - P0D
- D - DsECAL

The cosmic trigger algorithm requires double coincidence from any two of the 6 sides of this rectangular box to generate a global cosmic trigger. There are 15 combinations of side pairs from the 6 sides of this trigger rectangular box, which are labeled as following: Top-Left, Top-Bottom, Top-Right, Top-P0D, Top-DsEcal, Left-Bottom, Left-Right, Left-P0D, Left-DsEcal, Bottom-Right, Bottom-P0D, Bottom-DsEcal, Right-P0D, Right-DsEcal, and P0D-DsEcal.

Each of these particular combinations can be used to select cosmic events which traverse specific parts of the ND280 off-axis detector. Here we are particularly interested in those triggers that traverse any part of the SMRD. The only trigger combination not useful to the SMRD is PD (P0D and DsECAL) as it strikes none of the faces of the SMRD.

[3]The P0D and DsECAL triggering mechanism is not discussed in detail as it is unnecessary for a discussion of the SMRD cosmic trigger settings

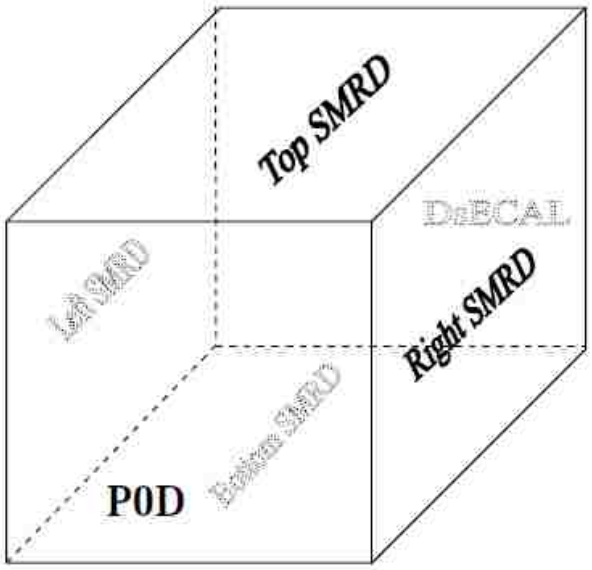

Figure 5.1: The above diagram shows the ND280 detector as a rectangular solid with each side labeled according to it cosmic trigger.

5.2 Data Sample Selection

The first selection criteria for a hit occurring in the SMRD is that this hit must be from a Trip-t cosmic event as described in the previous section. Once we know the hit is a TRip-t cosmic event we also want to make sure that the SMRD Data Quality Flag has been marked as good. If there are any periods where the SMRD has a known problem then we would choose to exclude those periods and this is done by processing only data that has the SMRD Data Quality Flag set to good.

Also the sample of data must be large enough for a reasonable statistical fit. How large is statistically significant? Seeing that we would like to have 30 hits per counter (recall there are 2008 counters) after making the cuts described below then we will need a data set that allows us to have a minimum of 60,240 hits after each of the following selection criteria is applied - this is assuming that all hits are evenly distributed which in practice is not the case. The 30 hits per counter requirement allows us to determine if the light yield of a single hit is near the mean or an outlier with respect to the mean. The mean of a sample of measurements becomes dominant as more measurements are taken, and therefore more is better as it yields a more stringent value on the mean. Hence, we need measurement sample large enough to determine how statistically significant any one measurement is.

5.2.1 SMRD Trigger Selection

Unbiased Trigger

An unbiased trigger is defined as any trigger that strikes that face of the ND280 regardless of which second face of the ND280 is triggered. For example, if we wanted an unbiased trigger for horizontal counters in the SMRD we would select any trigger that includes T or B (Top or Bottom) faces triggering. However, if we are interested in the horizontal counters we want to make sure that we are only looking at light yields due to muon hit in horizontal counters. In other words, even though we will include a TL trigger as part of an unbiased trigger sample for horizontal counters, we only wan to to consider the light yield due to the hits in the top of the detector while excluding the hits int left face of the SMRD.

The reverse would be true for an unbiased sample for vertical counters. While we could still use the TL trigger we only want the hits occurring in the left side of the SMRD while excluding those in the top of the SMRD.

Top-Bottom and Side-Side Triggers

For a TB (Top-Bottom) trigger we want only those tracks that traverse the top and bottom faces of the detector, but in this case we want to consider the light yield form both the hits in the top and in the bottom faces of the detector.

A similar selection can be made for SS (Side-Side) triggers[4] where both sides of the SMRD having vertical counters have triggered. As in the TB trigger, we only want to consider the light yield from the located on the sides of the SMRD where the counters are vertical in orientation.

5.2.2 Geometric Selection

It is well known that increased path length in a scintillator results in more energy deposited and hence greater light yield. For the SMRD path length is increased as the incoming cosmic ray muon crosses the counter at angle further away from the perpendicular. Hence, not all muons traversing the counter will have the same path length and thus not all muons of equal energy will produce the same light yield as their path length may vary. As reference axis we use the X-axis for vertical counters and the Y-axis for horizontal counters in order to determine angular separation.

In order to determine the angular separation from the reference axis we first do a simple track reconstruction. First we find all the hits in a track and then find the highest and lowest hits. Once we have the locations of the highest and lowest hits in the track we can build a line and compare the angular separation of the fitted track to the reference axis. This angular separation is then associated with each hit in the track. In order to pick hits with similar light yield we pick those that have similar angular separation as tracks with the same angular separation will have the same path length and thus nearly the same light yield.

[4]There is no particular distinction between LR and RL triggers.

5.3 Light Yield for an Unbiased Trigger

For the plot shown in Fig. 5.2 we have seperated horizontal counters (shown as the red dashed line) from vertical counters (shown as the blue line). Here we have used an unbiased trigger as described above and there are no geometrical selection parameters. As there are no geometrical selection parameters then the path length can vary from the minimum to the maximum.

Recall that the vertical counters are slightly larger in size and thus it is possible for the maximum path length of a muon in a vertical counter to be greater than the maximum path length in a horizontal counter. This geometry difference in the vertical counters could lead to a higher light yield.This evidenced by the higher mean value of the light yield for the vertical counters as compared to that of the horizontal counters, 112.8 $\pm$ 0.3 p.e. vs. 100.7 $\pm$ 0.5 p.e. respectively. The data for this plot is taken from run 7508 and includes 88 sub-runs while the time length of the data set is 22.03 hours during 1/18 to 1/19 of 2011.

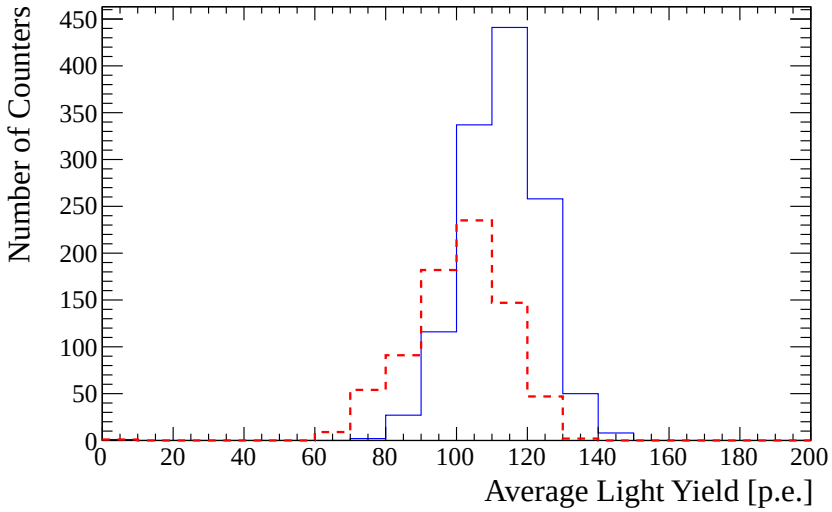

Figure 5.2: Light Yield of horizontal (red dashed line) versus vertical counters (blue solid line) for an unbiased trigger sample.

5.4 Light Yield for Geometrically Equivalent Top-Bottom and Side-Side Triggers

At this point we wish to use several cuts combined in order to look at the light yield from hits that have nearly the same path length. First, we choose a trigger type, in this case TB, and we require that a hit must occur in either a counter on the top of the the detector or the bottom of the detector. The second requirement is necessary because although the trigger may be TB there is the possibility that incidental hits in the side counters may be included if they occur during the time interval while the top and bottom are triggered. For this particular data set of run 7508 inclusive of all 88 sub-runs this happens for $\sim$2% of hits with a TB trigger.

In addition to the previously mentioned cuts we require that the angular separation for the track associated with the hit be $\leq 10^{\circ}$. In the case of the horizontal counters the Y-axis is perpendicular and if we were

the traverse the counter directly down the Y-axis the path length traversed would be the thick ness of the counter - 7 mm. Being separated at most by 10° changes the path length to 7.11 mm while increasing the number of hits per counter to a statistically significant amount of 30 hits per counter or more.

The resulting distribution is shown in Fig. 5.3 with a mean value of 79.6 ± 0.5. This value is significantly lower than the unbiased version due to the limit in the path length via the requirement that the associated angular separation be $\leq 10°$.

We would like to repeat the process for the SS, i.e. LR or RL, trigger but there is a problem. In the TB trigger we required a minimum of 30 hits per counter. For SS triggers there are significantly less tracks within 10° of the perpendicular X-axis. In fact less than 1% of counters have 10 or more hits yielding a poor statistical fit for those counters. The solution would be to use a larger data set. While a search for a usable data set of manageable size has been conducted none have been found to date.

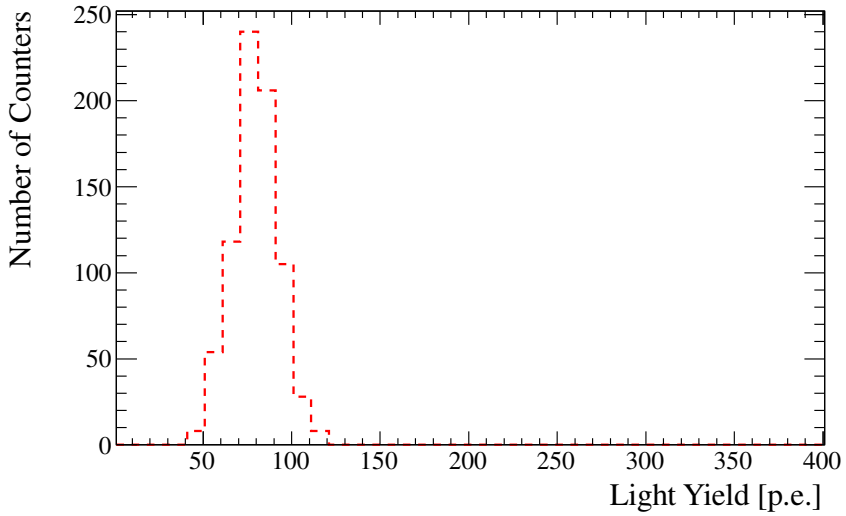

Figure 5.3: Run 7508 using 88 subruns during 1/18-19/2011. Top-Bottom trigger only hits must be within 10° of the Y-axis and occur in a horizontally oriented counter.

5.5 Light Yield Over Time

What we would like to do is to produce a light yield over time plot this seems quite simple. We would like to replicate what we did for the TB trigger plots in the previous section, but instead of doing for on small period in time do it for may small period in time. In other words we would like to make the previous plot for every available 24 hour period of data, extract the mean value of the distribution, and then plot those mean values on a light yield vs. time graph. However, the difficulty again lies in efficient use of the data. Processing time has been calculated to be on the order of weeks, and if multiple iterations need be done as is often the case then it could be months. So effort is best invested in finding a way to efficiently work with the data to be processed.

As a preliminary step we have been able to take the arithmetic mean of all hits meeting selection requirement that occur in a 24 hour period and plot those averages over time. Shown in Fig. 5.4 the averages for any hit taken during that 24 hour period where the light yield values are required to less than 400 p.e.

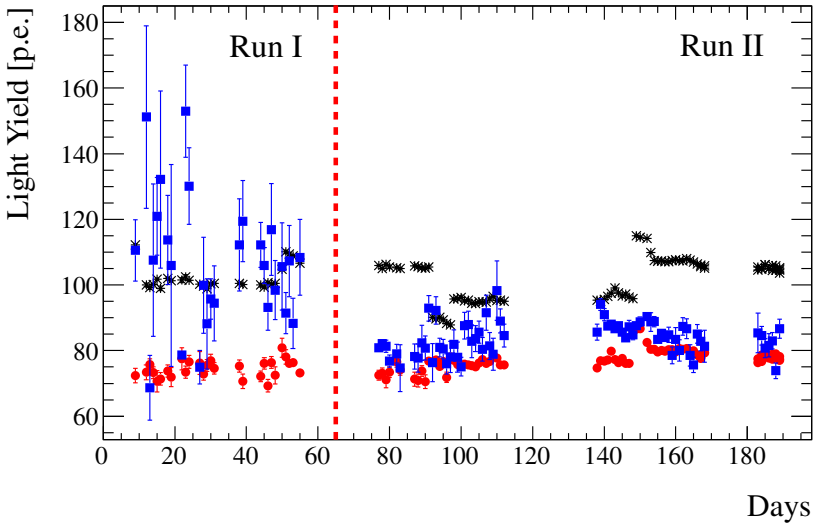

Figure 5.4: Light Yield per 24 Hour period plotted from March of 2010 through March 2011 where the time scale is measured in days of data acquired. The asterisks (black) represent all triggers in any counter, while the circular data points are for TB triggers with only hits in horizontal counters limited to within 10° of the Y-axis. Likewise, the square data points are for SS triggers with only hits in vertical counters limited to within 10° of the X-axis

are shown as data point marked by asterisks (black). Values here are sporadic as any path length in any direction is allowed with no requirement on the minimum number of hits during a 24 hour period.

In direct comparison are the data points represented by the circular (red) markers. These data points are TB triggers only and are averaged over a 24 hour period as are all of the other data points. We also require that any hit must occur in horizontal counter and its associated angular separation from the Y-axis must be $\leq 10°$. This produces better results with a narrower range of values. Their are however several minor shifts and these values need to be investigated further. They may disappear once we can instantiate the original idea making sure that we have an statistically significant amount of hits per counter.

Lastly, we have the data points represented by the square (blue) markers. These data points are SS triggers only and are averaged over a 24 hour period as are all of the other data points. We also require that any hit must occur in vertical counter and its associated angular separation from the X-axis must be $\leq 10°$. Although the values in Run II are quite stable the values in Run I are the most sporadic of all data points on this plot. The larger error bars on the Run I SS data points stem from the fact that there are so few hits per 24 hour period meeting the cut requirements. So why are the 24 hour average values for SS hits more stable in Run II?

Looking at Table 5.1 we see that there are significant differences in the percentage of types of hits in Run I vs. Run II. It should be noted that the tracks listed as Top, Bottom, Left, and Right on Table 5.1 are tracks that have used only on side of the SMRD to create TFB cosmic trigger and therefore the other side used in the TFB cosmic trigger must be either the P0D or the DsECAL. It can be seen that Top triggers and the Bottom triggers combined account for ∼35% of all hits in Run I, but North and South triggers combined account for <1% of all triggers. Based on the location of hits in Run I these type of hits will have associated track angles greater than 10° causing them to have greater light yield. Comparatively, in Run II hits from Top, Bottom, North and South triggers are each ∼4% of the total hits.

Additionally, as can be seen in Fig. 5.4, the average values for hits occurring in a Top-Bottom trigger, marked by the circular (red) data points, have a lower light yield than the overall average, marked by the asterisk (black) data points. However, it should also be noted that the Top-Bottom triggers only account for ∼7% of triggers in Run I. In contrast, hits occurring as part of a Top-Bottom trigger in Run II account for nearly 20% of all hit during Run II.

It is in fact the Side-Side triggers that account for the largest percentage, nearly one third, of triggers of any one type. However, further investigation has found that the trigger masks were set during Run I such that the vast majority of recorded Side-Side triggers traversed the longest possible diagonal of the ND280 detector. More specifically, most Side-Side triggers occurred when an upstream corner of the SMRD was triggered in coincidence with the opposing downstream corner of the SMRD. For example, a vertical counter on the upper left of Yoke 1 (upstream) in the SMRD would initialize the cosmic trigger and a vertical counter on the lower right of Yoke 8 (downstream) would finalize the trigger. Hence very few of the Side-Side triggers in Run I meet the cut requirement that the associated angular separation from the X-axis must be $\leq 10°$.

Likewise, in Run II it is the hits from the Side-Side triggers that dominate, but these hits are distributed across the SRMD giving many more hits that meet our angular requirement. This clearly demonstrated by the less sporadic Side-Side average values in Fig. 5.4 and the smaller error bars that accompany them.

Overall we can say that both hits from different trigger types ar more evenly distributed during Run II than in Run I. The physical location of hits in the SMRD is also more evenly distributed across the entire SMRD during Run II than in Run I. Consequently, this leads to the increased stability seen in Run II when compared to Run I. However, the overall average light yield is stable to within roughly 10% over both Run I and Run II.

Table 5.1: The table below shows the percentage of types triggers in Run I versus those in Run II.

Trigger Type	**Hits for Run I**	**% of Run I Hits**	**Hits for Run II**	**% of Run II Hits**
Top	299,853	19.64042	920,564	4.3671
Bottom	245,962	16.11055	799,667	3.793572
North	6,700	0.438851	812,752	3.855646
South	6,047	0.396079	808,786	3.836832
Top-North	62,656	4.103978	2,103,865	9.980608
Top-South	56,671	3.711959	2,010,206	9.536296
Top-Bottom	106,350	6.965941	4,149,580	19.68536
Side-Side	484,218	31.71635	5,652,252	26.81394
North-Bottom	9,317	0.610265	623,422	2.957476
South-Bottom	35,556	2.328923	1,443,675	6.848707
Misplaced Hits[5]	213,384	13.97668	1,754,758	8.324466
Total	1,526,714	100	21,079,527	100%

[5]Misplaced hits are hits that occur in locations other than those corresponding to the trigger type. For example, if a cosmic event has a Top-Bottom trigger, then any hit during that event that occurs in a side wall of the SMRD would be considered a "misplaced hit".

Chapter 6

Summary and Conclusion

Initially, we presented an historical overview of neutrino physics, starting from Pauli's initial proposal of the neutrino on through to some of the open questions in neutrino physics today. While so doing some basics in regards to the mathematical description of neutrino oscillations were also presented.

Afterwards, an overview of the T2K experiment was presented. As it is the primary goal of the T2K experiment to measure the mixing angle θ_{13}, we looked at not only the mathematical basis for an oscillation of ν_μ to ν_e but also the physical setup to do so. The T2k experiment is up and running but is in the early stages of the experiment. We looked at a general overview of the production of the neutrino beam and of the far detector Super-K in order to understand their roles in T2K. Much of the discussion regarding the physical setup of the experiment focused on the ND280 near detector as this is where the neutrino beam is characterized prior to oscillation.

Next, the overall role of the SMRD as it functions in the ND280 was presented. Recall that the three main functions of the SMRD are:

1. the SMRD measures muons produced in neutrino interactions that cannot be well reconstructed by the detectors located in the tracker section,
2. the SMRD detects cosmic ray muons for the purpose of calibration triggering, and
3. it vetoes muons that come from sources outside of the ND280.

After establishing the function of the SMRD we discussed how its design met physical constraints while satisfying the above mentioned function.

We presented data quality concerns for the SMRD and presented which parameters are examined to determine whether the period of data taken qualifies as "good". We used the data quality flag to examine the fraction of time that the SMRD has been considered to be operating with in expected parameters and found that more than 99% of the time available the SMRD was flagged as good.

In regards to the future outlook for data quality, not only will the afore described checks continue, but in the very near future we plan to add automated efficiency checks. The goal will be to track on a regular

basis how often the SMRD registers hits as compared to how often it should be registering hits, i.e. how well it detects what it should.

Lastly, the first attempt to show detector stability was presented. While so promising results have been achieved there is more to be done. Currently, in progress is an attempt to extract the mean values of each of the 2008 counters for the all of the months of data available, as was done for the the small data set that focused on light yield in horizontal counters from Top-Bottom triggers [see Section 5.4]. Current attempts are very slow to process as the data set is quite large, the key is to find the most efficient way to process this large data set such that the required CPU time is reasonable. This will be the culmination of detector stability.

Bibliography

[1] K. Abe, N. Abgrall, H. Aihara, Y. Ajima, J.B. Albert, D. Allan, P.-A. Amaudruz, C. Andreopoulos, B. Andrieu, M.D. Anerella, C. Angelsen, S. Aoki, O. Araoka, J. Argyriades, A. Ariga, T. Ariga, S. Assylbekov, J.P.A.M. de Andr, D. Autiero, A. Badertscher, O. Ballester, M. Barbi, G.J. Barker, P. Baron, G. Barr, L. Bartoszek, M. Batkiewicz, F. Bay, S. Bentham, V. Berardi, B.E. Berger, H. Berns, I. Bertram, M. Besnier, J. Beucher, D. Beznosko, S. Bhadra, P. Birney, D. Bishop, E. Blackmore, F.d.M. Blaszczyk, J. Blocki, A. Blondel, A. Bodek, C. Bojechko, J. Bouchez, T. Boussuge, S.B. Boyd, M. Boyer, N. Braam, R. Bradford, A. Bravar, K. Briggs, J.D. Brinson, C. Bronner, D.G. Brook-Roberge, M. Bryant, N. Buchanan, H. Budd, M. Cadabeschi, R.G. Calland, D. Calvet, J. Caravaca Rodrguez, J. Carroll, S.L. Cartwright, A. Carver, R. Castillo, M.G. Catanesi, C. Cavata, A. Cazes, A. Cervera, J.P. Charrier, C. Chavez, S. Choi, S. Chollet, G. Christodoulou, P. Colas, J. Coleman, W. Coleman, G. Collazuol, K. Connolly, P. Cooke, A. Curioni, A. Dabrowska, I. Danko, R. Das, G.S. Davies, S. Davis, M. Day, X. De La Broise, P. de Perio, G. De Rosa, T. Dealtry, A. Debraine, E. Delagnes, A. Delbart, C. Densham, F. Di Lodovico, S. Di Luise, P. Dinh Tran, J. Dobson, J. Doornbos, U. Dore, O. Drapier, F. Druillole, F. Dufour, J. Dumarchez, T. Durkin, S. Dytman, M. Dziewiecki, M. Dziomba, B. Ellison, S. Emery, A. Ereditato, J.E. Escallier, L. Escudero, L.S. Esposito, W. Faszer, M. Fechner, A. Ferrero, A. Finch, C. Fisher, M. Fitton, R. Flight, D. Forbush, E. Frank, K. Fransham, Y. Fujii, Y. Fukuda, M. Gallop, V. Galymov, G.L. Ganetis, F.C. Gannaway, A. Gaudin, J. Gaweda, A. Gendotti, M. George, S. Giffin, C. Giganti, K. Gilje, I. Giomataris, J. Giraud, A.K. Ghosh, T. Golan, M. Goldhaber, J.J. Gomez-Cadenas, S. Gomi, M. Gonin, M. Goyette, A. Grant, N. Grant, F. Graena, S. Greenwood, P. Gumplinger, P. Guzowski, M.D. Haigh, K. Hamano, C. Hansen, T. Hara, P.F. Harrison, B. Hartfiel, M. Hartz, T. Haruyama, R. Hasanen, T. Hasegawa, N.C. Hastings, S. Hastings, A. Hatzikoutelis, K. Hayashi, Y. Hayato, T.D.J. Haycock, C. Hearty, R.L. Helmer, R. Henderson, S. Herlant, N. Higashi, J. Hignight, K. Hiraide, E. Hirose, J. Holeczek, N. Honkanen, S. Horikawa, A. Hyndman, A.K. Ichikawa, K. Ieki, M. Ieva, M. Iida, M. Ikeda, J. Ilic, J. Imber, T. Ishida, C. Ishihara, T. Ishii, S.J. Ives, M. Iwasaki, K. Iyogi, A. Izmaylov, B. Jamieson, R.A. Johnson, K.K. Joo, G. Jover-Manas, C.K. Jung, H. Kaji, T. Kajita, H. Kakuno, J. Kameda, K. Kaneyuki, D. Karlen, K. Kasami, V. Kasey, I. Kato, H. Kawamuko, E. Kearns, L. Kellet, M. Khabibullin, M. Khaleeq, N. Khan, A. Khotjantsev, D. Kielczewska, T. Kikawa, J.Y. Kim, S.-B. Kim, N. Kimura, B. Kirby, J. Kisiel, P. Kitching, T. Kobayashi, G. Kogan, S. Koike, T. Komorowski, A. Konaka, L.L. Kormos, A. Korzenev, K. Koseki, Y. Koshio, Y. Kouzuma, K. Kowalik, V. Kravtsov, I. Kreslo, W. Kropp, H. Kubo, J. Kubota, Y. Kudenko, N. Kulkarni, L. Kurchaninov, Y. Kurimoto, R. Kurjata, Y. Kurosawa, T. Kutter, J. Lagoda, K. Laihem, R. Langstaff, M. Laveder, T.B. Lawson, P.T. Le, A. Le Coguie, M. Le Ross, K.P. Lee, M. Lenckowski, C. Licciardi, I.T. Lim, T. Lindner, R.P. Litchfield, A. Longhin, G.D. Lopez, P. Lu, L. Ludovici, T. Lux, M. Macaire, L. Magaletti, K. Mahn, Y. Makida, C.J. Malafis, M. Malek, S. Manly, A. Marchionni, C. Mark, A.D. Marino, A.J. Marone, J. Marteau, J.F. Martin, T. Maruyama, T. Maryon, J. Marzec, P. Masliah, E.L. Mathie, C. Matsumura, K. Mat-

suoka, V. Matveev, K. Mavrokoridis, E. Mazzucato, N. McCauley, K.S. McFarland, C. McGrew, T. McLachlan, I. Mercer, M. Messina, W. Metcalf, C. Metelko, M. Mezzetto, P. Mijakowski, C.A. Miller, A. Minamino, O. Mineev, S. Mine, R.E. Minvielle, G. Mituka, M. Miura, K. Mizouchi, J.-P. Mols, L. Monfregola, E. Monmarthe, F. Moreau, B. Morgan, S. Moriyama, D. Morris, A. Muir, A. Murakami, J.F. Muratore, M. Murdoch, S. Murphy, J. Myslik, G. Nagashima, T. Nakadaira, M. Nakahata, T. Nakamoto, K. Nakamura, S. Nakayama, T. Nakaya, D. Naples, B. Nelson, T.C. Nicholls, K. Nishikawa, H. Nishino, K. Nitta, F. Nizery, J.A. Nowak, M. Noy, Y. Obayashi, T. Ogitsu, H. Ohhata, T. Okamura, K. Okumura, T. Okusawa, C. Ohlmann, K. Olchanski, R. Openshaw, S.M. Oser, M. Otani, R.A. Owen, Y. Oyama, T. Ozaki, M.Y. Pac, V. Palladino, V. Paolone, P. Paul, D. Payne, G.F. Pearce, C. Pearson, J.D. Perkin, M. Pfleger, F. Pierre, D. Pierrepont, P. Plonski, P. Poffenberger, E. Poplawska, B. Popov, M. Posiadala, J.-M. Poutissou, R. Poutissou, R. Preece, P. Przewlocki, W. Qian, J.L. Raaf, E. Radicioni, K. Ramos, P. Ratoff, T.M. Raufer, M. Ravonel, M. Raymond, F. Retiere, D. Richards, J.-L. Ritou, A. Robert, P.A. Rodrigues, E. Rondio, M. Roney, M. Rooney, D. Ross, B. Rossi, S. Roth, A. Rubbia, D. Ruterbories, R. Sacco, S. Sadler, K. Sakashita, F. Sanchez, A. Sarrat, K. Sasaki, P. Schaack, J. Schmidt, K. Scholberg, J. Schwehr, M. Scott, D.I. Scully, Y. Seiya, T. Sekiguchi, H. Sekiya, G. Sheffer, M. Shibata, Y. Shimizu, M. Shiozawa, S. Short, M. Siyad, D. Smith, R.J. Smith, M. Smy, J. Sobczyk, H. Sobel, S. Sooriyakumaran, M. Sorel, J. Spitz, A. Stahl, P. Stamoulis, O. Star, J. Statter, L. Stawnyczy, J. Steinmann, J. Steffens, B. Still, M. Stodulski, J. Stone, C. Strabel, T. Strauss, R. Sulej, P. Sutcliffe, A. Suzuki, K. Suzuki, S. Suzuki, S.Y. Suzuki, Y. Suzuki, Y. Suzuki, J. Swierblewski, T. Szeglowski, M. Szeptycka, R. Tacik, M. Tada, A.S. Tadepalli, M. Taguchi, S. Takahashi, A. Takeda, Y. Takenaga, Y. Takeuchi, H.A. Tanaka, K. Tanaka, M. Tanaka, M.M. Tanaka, N. Tanimoto, K. Tashiro, I.J. Taylor, A. Terashima, D. Terhorst, R. Terri, L.F. Thompson, A. Thorley, M. Thorpe, W. Toki, T. Tomaru, Y. Totsuka, C. Touramanis, T. Tsukamoto, V. Tvaskis, M. Tzanov, Y. Uchida, K. Ueno, M. Usseglio, A. Vacheret, M. Vagins, J.F. Van Schalkwyk, J.-C. Vanel, G. Vasseur, O. Veledar, P. Vincent, T. Wachala, A.V. Waldron, C.W. Walter, P.J. Wanderer, M.A. Ward, G.P. Ward, D. Wark, D. Warner, M.O. Wascko, A. Weber, R. Wendell, J. Wendland, N. West, L.H. Whitehead, G. Wikstrm, R.J. Wilkes, M.J. Wilking, Z. Williamson, J.R. Wilson, R.J. Wilson, K. Wong, T. Wongjirad, S. Yamada, Y. Yamada, A. Yamamoto, K. Yamamoto, Y. Yamanoi, H. Yamaoka, C. Yanagisawa, T. Yano, S. Yen, N. Yershov, M. Yokoyama, A. Zalewska, J. Zalipska, K. Zaremba, M. Ziembicki, E.D. Zimmerman, M. Zito, and J. Zmuda. The t2k experiment. *Nuclear Instruments and Methods in Physics Research Section A: Accelerators, Spectrometers, Detectors and Associated Equipment*, 659(1):106 – 135, 2011.

[2] Ernest Rutherford, James Chadwick, and C.D. Ellis. *Radiations from Radioactive Substances*. Macmillan Publishing Co., 1930.

[3] Laurie M. Brown. The idea of the neutrino. *Phys. Today*, 31N9:23–28, 1978.

[4] M.F. L'Annunziata. *Radioactivity: Introduction and History*. Elsevier, 2007.

[5] E. Fermi. An attempt of a theory of beta radiation. 1. *Z. Phys.*, 88:161–177, 1934.

[6] Fred L. Wilson. Fermi's theory of beta decay. *American Journal of Physics*, 36:1150, 1968.

[7] G. Danby, J.-M. Gaillard, K. Goulianos, L. M. Lederman, N. B. Mistry, M. Schwartz, and J. Steinberger. Observation of High-Energy Neutrino Reactions and the Existence of Two Kinds of Neutrinos. *Phys. Rev. Lett.*, 9:36–44, 1962.

[8] K. Kodama et al. Observation of tau-neutrino interactions. *Phys. Lett.*, B504:218–224, 2001.

[9] Nobelprize.org. The nobel prize in physics 2002, April 2012.

[10] V. N. Gribov and B. Pontecorvo. Neutrino astronomy and lepton charge. *Phys. Lett.*, B28:493, 1969.

[11] W. David Arnett and Jonathan L. Rosner. NEUTRINO MASS LIMITS FROM SN1987a. *Phys. Rev. Lett.*, 58:1906, 1987.

[12] Q. R. Ahmad et al. Measurement of the charged current interactions produced by B-8 solar neutrinos at the Sudbury Neutrino Observatory. *Phys. Rev. Lett.*, 87:071301, 2001.

[13] A. B. McDonald, J. R. Klein, and D. L. Wark. Solving the solar neutrino problem. *Sci. Am.*, 288N4:40–49, 2003.

[14] E. Kearns, T. Kajita, and Y. Totsuka. Detecting massive neutrinos. *Sci. Am.*, 281N2:48–55, 1999.

[15] B. Pontecorvo. Mesonium and anti-mesonium. *Zh. Eksp. Teor. Fiz.*, 33:549551, 1957.

[16] Z. Maki, M. Nakagawa, and M. Sakata. Remarks on the unified model of elementary particles. *Progress of Theoretical Physics*, 28(5):870–880, 11 1962.

[17] B. Pontecorvo. Neutrino experiments and the problem of conservation of leptonic charge. *Zh. Eksp. Teor. Fiz.*, 53:1717, 1967.

[18] Jr. Davis, Raymond, Don S. Harmer, and Kenneth C. Hoffman. Search for neutrinos from the sun. *Phys. Rev. Lett.*, 20:1205–1209, 1968.

[19] K. Nakamura et al. Review of particle physics. *J. Phys.*, G37:075021, 2010.

Vita

Jeremiah J. Haremza was born at home in Littleton, Colorado to Christine Haremza. After moving to Buffalo, New York he attended high school at City Honors. After his freshman year at City honors he moved again to Lockport, New York where he graduated from Lockport High School in just two years.

After ten years in the corporate environment he was intellectually bored and decided to return to higher education. Initially he planned to spend two years at a community college and then finish his B.S. in physics at a state school as this route would be both in expensive and quick. After only one year at Niagara County Community College he was ready to move on and decided that the most intellectually stimulating option would be to pursue a double major at the University of Rochester.

In 2006 he began his double major in physics and philosophy. At the University of Rochester he studied differential geometry, particle physics, epistemology, the philosophies of Immanuel Kant, and assisted in building a low-field NMR device. Three years later he graduated from the University of Rochester with a B.S. in Physics with a minor in Mathematics as well as a B.A. In Philosophy. He received his Philosophy degree with highest honors (summa cum laude). While at the University of Rochester he was a teaching assistant in astronomy as well as taught test prep for The Princeton Review in MCAT Chemistry, GRE, GMAT, and SAT.

In 2009 he was offered a chance to continue his academic career at Louisiana state University (LSU) and began as both a graduate student and teaching assistant in the fall of that year. While at LSU he taught both astronomy and physics lab courses. In the summer of 2010 he began research with Dr. Thomas Kutter who lead an experimental group focusing on the Side Muon Range Detector (SMRD) of the Tokai to Kamiokande (T2K) experiment. Jeremiah would go on to develop the automation code for the data quality analysis of the SMRD which would constitute pat of his masters thesis. He would also work on the relation between temperature and event rates in the SMRD as well as the stability of the SMRD. He expects to receive his Masters Degree in the Summer of 2012.